https://doi.org/10.5194/egusphere-2026-4311
Preprint. Discussion started: 23 July 2026

Observing Seawater Flooding on Arctic First-Year Ice during Pre-Melt Using C- and L-Band Synthetic Aperture Radar

Constanza S. Salvó[1,2], Randall K. Scharien[3], David Iqqaqsaq[4], Robert Briggs[5], Trevor Bell[6,7], Saeid Homayouni[1,2]

[1] Centre Eau Terre Environnement, Institute National de la Recherche Scientifique, Québec, QC G1K 9A9, Canada
[2] Centre d'Études Nordique (CEN) d'Université Laval, Québec, QC G1V 0A6, Canada,
[3] Department of Geography, University of Victoria, Victoria, BC V8P 5C2, Canada
[4] SmartICE Monitoring & Information Inc, Qikiqtarjuaq, NU X0A 0B0, Canada
[5] National Research Council of Canada, St. John's, NL A1B 3T5, Canada
[6] SmartICE Monitoring & Information Inc, St. John's, NL A1A 5G9, Canada
[7] Department of Geography, Memorial University of Newfoundland, St. John's, NL A1C 5S7, Canada

Correspondence to: Constanza S. Salvó (constanza_sofia.salvo@inrs.ca)

Abstract

Seawater flooding from negative freeboard onto sea ice leads to the formation of a saline slush layer at the bottom of the snowpack, affecting snowpack geophysical properties, ice mass balance, remote sensing retrievals, and on-ice travel safety. Synthetic Aperture Radar (SAR) is sensitive to saline slush, though limited information on this dynamic layer exists. This research assesses the sensitivity of C- and L-band frequency SAR to slush occurrence on Arctic first-year ice near Qikiqtarjuaq (Nunavut, Canada) during pre-melt conditions and evaluates the potential of SAR to estimate flooding. SAR parameters backscatter, logarithm ratio, cross- and co-polarization ratios, coherence, and textural features, are evaluated for their ability to distinguish *Flooded* from *Non-flooded* classes and results are tested at a regional scale. The loss of coherence in co-polarization L-band SAR, due to the occurrence of a high-dielectric slush layer, is found to be optimal for flooding detection, with the lower frequency being less influenced by the overlying snow. Backscatter, and its temporal change through the logarithm ratio, consistently discriminates classes when the slush is refreezing or has frozen into snow ice. Regional-scale estimation using L-band coherence is demonstrated as achieving an F1-score of 0.81, with higher F1-scores (up to 0.87) obtained when random forest models combine textural information with coherence. These findings highlight the dynamic nature of seawater flooding, and the potential for SAR to be used in related applications and research studies.

1 Introduction

Seawater flooding at the snow-ice interface leads to the formation of a saline slush layer that alters the physical properties of snow and sea ice, impacting remote sensing applications such as snow and ice thickness estimation (Nandan et al., 2020; Rösel et al., 2021). When refreezing, slush consolidates into snow ice, contributing to the sea ice mass balance and modifying ice properties, the energy budget, and biological productivity (Fritsen et al., 1998; Jeffries et al., 2001; Saloranta, 2000). Flooded

https://doi.org/10.5194/egusphere-2026-4311
Preprint. Discussion started: 23 July 2026

sea ice is also visually challenging to detect, especially when the entire snowpack is not fully inundated, increasing the likelihood of over-snow vehicles such as snowmobiles becoming stuck and posing a travel safety hazard to people living in Arctic communities (Gusmeroli & Grosse, 2012; Segal et al., 2020b).

Seawater infiltration onto the ice surface normally occurs when the freeboard becomes negative, either because of increased snow loading (Arndt et al., 2017; Haas et al., 2001) or reduced ice thickness resulting from basal melting or current-induced erosion (Ackley et al., 2020; Arndt et al., 2017; Provost et al., 2017), which lowers the ice surface below the seawater level. In both cases, sea ice permeability plays a significant role by determining the ability of seawater to move upward and overflow onto the ice surface (Ackley et al., 2020; Jutras et al., 2016), increasing as brine channel networks develop at warmer ice temperatures (Drinkwater & Lytle, 1997). Lateral movement of seawater from openings such as cracks, regions of deformation, and floe edges is also relevant (Drinkwater & Lytle, 1997; Geilfus et al., 2023).

Studies on the detection and characterization of flooded ice using remote sensing have mainly focused on microwave energy, in particular radar. Ship-mounted radar studies reported that microwave signals are sensitive to saline slush during late winter to spring in Antarctica (Hosseinmostafa et al., 1995; Hosseinmostafa & Lytle, 1992; Jeffries et al., 1995). Hosseinmostafa et al. (1995) found a lower backscatter coefficient (σ^0) for slush-covered first-year ice (FYI), using a C-band (5.3 GHz) frequency radar operating in vertical transmit-receive (VV) polarization in the Weddell Sea. The slush layer additionally reduced the distinction between FYI and second-year ice, as well as smooth or rough ice (Hosseinmostafa et al., 1995; Hosseinmostafa & Lytle, 1992). The latter was attributed either to the effect of a smothering dielectric layer formed by the slush (Hosseinmostafa et al., 1995; Hosseinmostafa & Lytle, 1992), or to a possible roughening effect of slush on otherwise smooth surfaces (Hosseinmostafa & Lytle, 1992).

According to a microwave backscatter modeling analysis performed by Hosseinmostafa et al. (1995), the C-band VV σ^0 for slush-covered FYI is dominated by surface scattering and depends on the incidence angle. At incidence angles below 20°, VV σ^0 is increasingly sensitive to slush, showing higher values, whereas at larger incidence angles, slush moderately reduces σ^0 by 2-3 dB relative to non-flooded ice. The authors suggested there is a balance between the effect of the slush smoothing the surface but also increasing the dielectric constant from 3.5 to ~60, which explains why backscatter does not decrease further. Volume scattering contributions from overlying snow layers were only observed at incidence angles above 50°.

In the Amundsen Sea, a comparison was made between a 3.5-4 cm thick layer of brine-wetted snow at the snow-ice interface of FYI and 10-14 cm of slush thickness on FYI, using a ship-mounted C-band (5.3 GHz) scatterometer at HH and VV polarizations (Jeffries et al., 1995). σ^0 values of both surfaces were as high as those of deformed ice, due to increases in the dielectric constant of wet snow and the dielectric contrast between wet and dry snow (Jeffries et al., 1995). The brine-wetted snow surface, with a salinity 2 ppt higher than that of deeper slush, showed higher backscatter values from 15° to 50° incidence angle, except at 20°, where both surfaces had similar values. Additionally, backscatter from both surfaces decreased with increasing incidence angle; however, slush showed a monotonic decrease, whereas brine-wetted snow did not, possibly indicating that multiple scattering mechanisms beyond surface scattering were involved in the latter case.

https://doi.org/10.5194/egusphere-2026-4311
Preprint. Discussion started: 23 July 2026

Detection of seawater flooding using synthetic aperture radar (SAR) is limited and studies show diverse σ^0 responses. The C-band ERS-1 SAR showed higher VV σ^0 values for flooded FYI, similar to deformed ice, at 20–26° incidence angles during late winter in Antarctica (Morris & Jeffries, 1995). On the other hand, Williams et al. (2024) reported a reduction in HH σ^0 due to surface flooding in C-band Sentinel-1 images of multiyear ice in Antarctica in early autumn. Segal et al. (2020b) indicated that slush detection in the winter Arctic is not feasible based on a qualitative assessment of C-band Sentinel-1 Extra-Wide mode HH images, but suggested that polarimetric discriminators be explored due to their sensitivity to moisture and dielectric constant. Franke et al. (2025) found high backscatter values associated with slush on Antarctic landfast sea ice surrounding grounded icebergs in a Tandem-X band scene.

The above review highlights that studies focused on seawater flooding using radars show results that are mainly from Antarctica and do not provide a comprehensive enough characterization of the flooding event, or the dynamics of the slush layer, to enable understanding of backscatter. SAR systems can be potentially valuable for detecting seawater flooding; however, complex processes at the snow-ice and dry snow-slush interfaces, driven by variations in salinity and brine volume (Barber & Nghiem, 1999; Drinkwater & Lytle, 1997; Geldsetzer et al., 2009), refreezing (Drinkwater & Lytle, 1997), surface roughness (Dammann et al., 2018; Segal et al., 2020a), and snow water content in spring (Scharien et al., 2018; Zhou et al., 2024), can rapidly alter the dielectric properties of the medium. Detection becomes increasingly complex when considering the influence of SAR parameters, such as frequency, polarization, and incidence angle (Johansson et al., 2018; Shokr & Dabboor, 2024).

Identifying areas affected by seawater flooding in the landfast ice is highly relevant for informing safe travel in Inuit communities, as highlighted by the knowledge and experience of SmartICE Community Management Committees (Wilson et al., 2021), whose input guided the design of this research. Seawater flooding is challenging to detect whilst travelling on the ice as it is hidden under the snow. Earth Observation tools can be useful for providing near-real-time information and, specifically in polar environments where lack of daylight or cloud cover restrict the reliable use of optical-based sensors, SAR can be a potentially useful sensor to detect flooding events for community travel decision-making. In this research, we focused on landfast FYI to study slush dynamics and their relationship with SAR data acquisition, as these ice platforms are used for travel by northern communities. This paper addresses the overall objective of determining the sensitivity of C- and L-band SAR to seawater flooding and slush occurrence in late winter (pre-melt) Arctic FYI. For simplicity, the term *slush* is used hereafter to denote seawater flooding that occurs beneath the surface snow, at the snow-ice interface. Towards these objectives, the following research questions are addressed:

1) How do SAR-derived parameters vary with slush occurrence over time and space?
2) Which SAR-derived parameters are most sensitive to slush occurrence?
3) Can the probability of seawater flooding be predicted at a regional scale?

The paper is structured as follows. Section 2 outlines data and methods, including the study area, sampling strategy, and observed conditions (2.1); snowpack conditions and flooding distribution (2.2); SAR data processing and parameters derivation (2.3-2.4); selection of most sensitive parameters (2.5); and predictions at a regional scale (2.6). Section 3 presents the results

https://doi.org/10.5194/egusphere-2026-4311
Preprint. Discussion started: 23 July 2026

of flooding on C- and L-band SAR parameters and model outcomes. In Section 4, results are discussed and, in Section 5, concluding remarks are made.

2 Data and Methods

2.1 Study Area, Sampling Strategy and Observed Conditions

The study area for this research is the landfast FYI adjacent to the community of Qikiqtarjuaq (67°33′17″ N, 64°1′41″ W), located on Broughton Island, in Nunavut, Canada (Figure 1a) where reports from the community have previously identified the presence of saline slush, or '*massak*', in the late winter and spring (Ikirmiut Community Management Committee, 2023). To investigate slush formation and evolution in relation to SAR backscatter, the study took place during the period slush usually forms, with data collected specifically from 14 April to 8 May 2024. A snowfall event from 20 to 24 April contributed a snow load of approximately 29 cm, as evidenced by an increase in measured snow depth from 53 to 82 cm at the Environment and Climate Change Canada (ECCC) station at Qikiqtarjuaq Airport (Figure 1a, 2a). This event supported slush formation, as verified by co-author Iqqaqsaq, a Qikiqtarjuaq resident who actively monitors and reports on local sea ice conditions. Air temperature during the study period showed an overall positive warming trend typical of the late winter to early melt conditions, with daily mean values remaining below 0°C (Figure 2a).

Four study sites affected by surface flooding were visited between 26 April and 7 May 2024, with each site taking 2-3 days for sampling and ranging in distance from 6 to 30 km from Qikiqtarjuaq. Chronologically, sites were sampled as follows: Site 1 (26-28 April), Site 2 (29-30 April), Site 3 (2-3 May), Site 4 (4-6 May), and a revisit to Site 1 and 2 (7 May) (Figure 1a). Sites were located with the guidance of local knowledge, and by extensive scouting that involved careful digging to confirm the presence or absence of slush beneath the snow. No deformation or topographic features were observed on the ice at any of the sites. At each site, ice, snow, and slush thickness were measured every 25 m along two orthogonal transects each of 250 m, yielding 21 independent records with one overlapping central point. 2-3 Snow pits were sampled per site, including vertical profiles of temperature, density, and salinity (from melted density samples) at 3 cm intervals. Covering the area surrounding the orthogonal transects, additional snow depth and slush thickness measurements were made every 50 m, using a gridded sampling pattern. Depending on the site, the additional gridded surveyed area ranged between 0.07 and 0.27 km^2. The presence or absence of slush was additionally noted opportunistically while traveling to, or searching for, sites, hereafter referred to as 'opportunistic records'.

On 28 April, two 12-bit Temperature Smart Sensors (S-TMB-M002, accuracy ±0.2°C) were installed at Site 1, one in a basal slush layer and the other 2 cm below the snow surface (Figure 1b). On 2 May, the sensors were inspected to assess performance and reinstalled adjacent to their original locations, where data were recorded until 7 May. Air temperature measurements for the entire study period at 10 m height, along with sea-level pressure and sky conditions, were recorded hourly at the nearby Qikiqtarjuaq ECCC station, and air temperature at near-surface (standing) height was recorded at each site using a Hanna HI98501 Electronic Thermometer with ±0.2°C accuracy. The ECCC recorded air temperature ranged from

https://doi.org/10.5194/egusphere-2026-4311
Preprint. Discussion started: 23 July 2026

-19.8°C to 0.5°C, remaining above -5°C on the morning of 28 April, the evening of 5 May, and from the evening to midnight on 6 and 7 May (Figure 2b). Differences in air temperature between the ECCC station and measured at-site reached up to 9.5°C, with lower values found at the weather station (Figure 2b).

The snow temperature evolution followed diurnal variations and a general warming trend typical of the pre-melt or early melt period preceding melt onset (Yackel et al., 2007), with a daily temperature amplitude of 7-14°C (Figure 2c). The slush temperature steadily decreased from -1.9°C to -2.3°C (Figure 2c). Snow layer temperatures from the snow pits at each site were below the freezing point (Millero & Leung, 1976), confirming the absence of snow melt. Nevertheless, the temperature sensor at Site 1 recorded ≥ 0°C in the late afternoons local time starting from 5 May (Figure 2c).

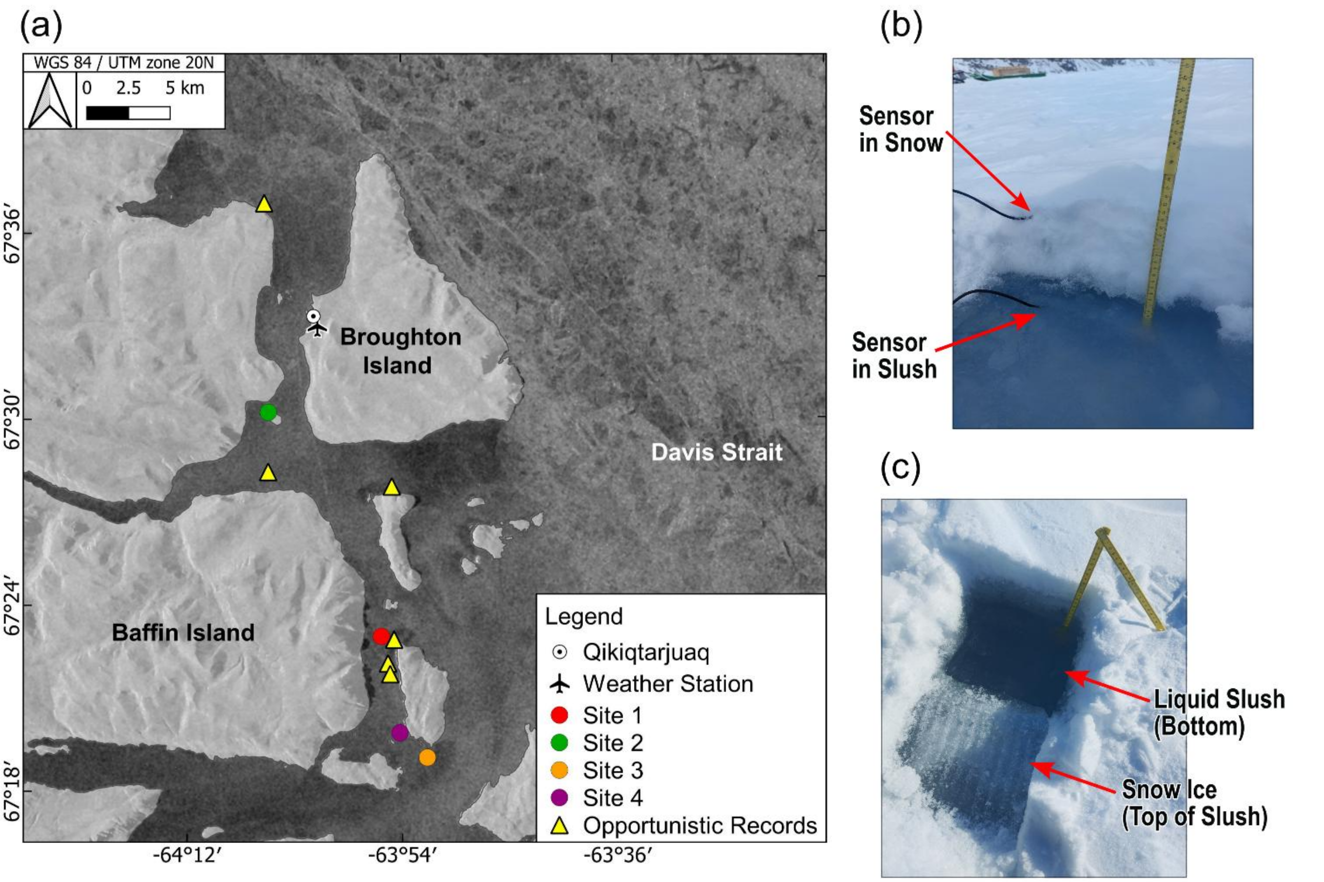

Figure 1: (a) Map of Qikiqtarjuaq on Broughton Island showing the location of sites with a RADARSAT Constellation Mission © Government of Canada (2024) horizontal transmit-receive (HH) image from 4 May 2024 as background. RADARSAT is an official mark of the Canadian Space Agency. (b) pit with slush showing the temperature sensor location in the snowpack profile at Site 1, (c) pit with slush refreezing, exposing at the bottom the liquid saline slush and at the top the snow ice layer.

https://doi.org/10.5194/egusphere-2026-4311
Preprint. Discussion started: 23 July 2026

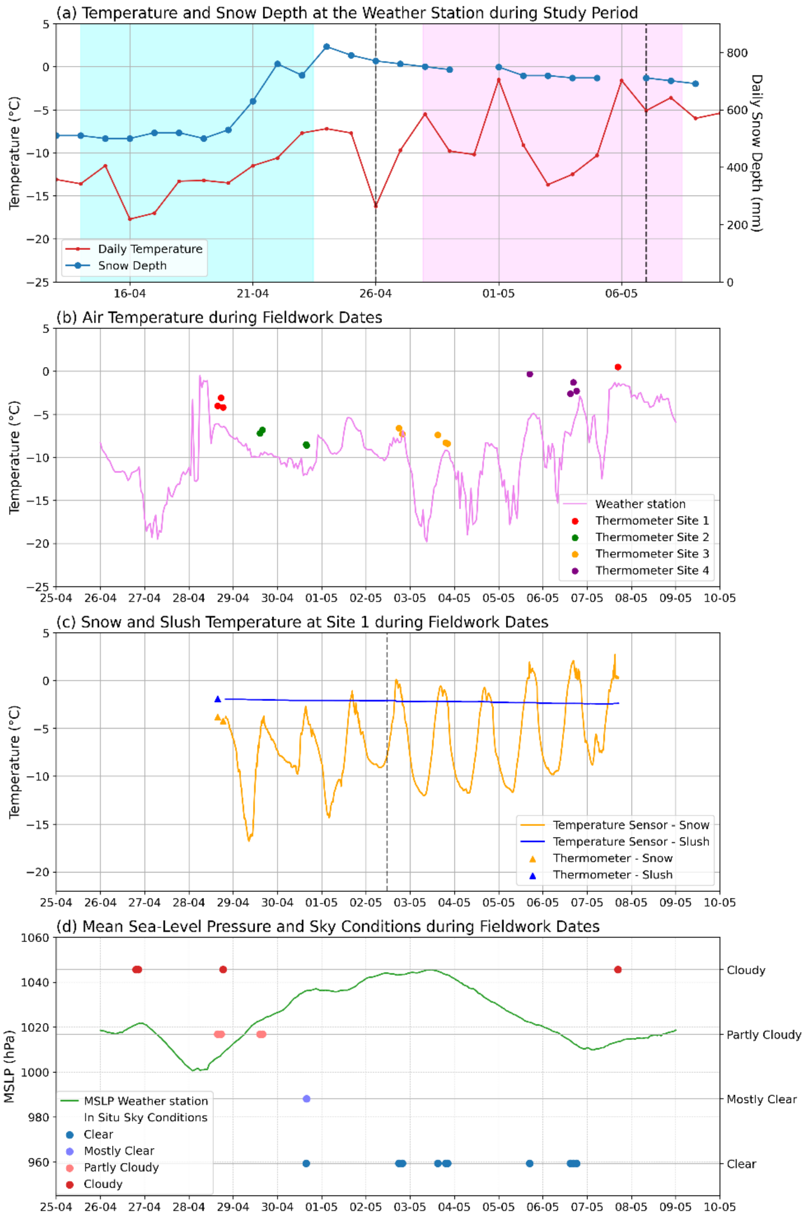

Figure 2: (a) Daily average air temperature (°C) and snow depth (mm) from the Qikiqtarjuaq ECCC weather station during the study period. The cyan background represents the period of t1 SAR acquisitions, and the magenta background represents the t_2 acquisitions (Table 2). Dashed lines indicate the first and last days of fieldwork. (b) Air temperature (°C) during fieldwork dates from the Qikiqtarjuaq ECCC weather station (line) and from measurements taken with a hand-held thermometer shown for Sites 1-4 (points). (c) Snow temperature (°C) near the air-snow interface and slush temperature near the snow-ice interface (°C) measured at site 1 using sensors (line) and hand-held thermometer (points) during fieldwork dates. The vertical dashed line when the sensor was inspected and reinserted. (d) Mean Sea Level Pressure (MSLP) in hectopascal and sky conditions from the Qikiqtarjuaq ECCC weather station during fieldwork dates.

https://doi.org/10.5194/egusphere-2026-4311
Preprint. Discussion started: 23 July 2026

2.2 Snowpack Conditions and Flooding Distribution

Four main snowpack conditions were found, described from the top-down (Figure 3a): i) *dry snow* to depth, with no slush; ii) dry snow with *saline slush* in liquid phase; iii) dry snow with slush *refreezing*, where it is evident that, overall, a transition to snow ice is occurring, with a snow ice layer at the top of the slush layer, hard but easily extractable when digging (Figure 1c); and iv) dry snow with *snow ice*, re-refrozen slush, solid and less extractable when digging. Because snow ice is solid, there was uncertainty about its thickness during digging, so layer thickness is not considered for this case. Snow ice formation was observed to occur from the top-down (also see Figure 1c).

Considerable variability in snow classes was observed during primary site visits, site revisits, and transit to and from the primary sites. Most notably, short-term transitions from slush to re-freezing and from re-freezing to snow ice. *Slush* and *dry snow* conditions were found at Sites 1 and 2. *Refreezing* and *snow ice* conditions were first observed on 2 May at Site 3 and subsequently observed on 3 May at Site 4, during revisits to Sites 1 and 2, and in opportunistic records (Figure 3b). Air temperatures below -5°C from the afternoon of 28 April (Figure 2b), together with clearing and clear skies starting on 30 April driven by an increase in mean sea level pressure (Figure 2c), likely contributed to a longwave radiative flux loss to the atmosphere and top-down refreezing of slush in the study area (Scharien et al., 2010). At Site 1, slush at the sensor position also showed a gradual decrease in snow temperature at the base of the snowpack from -1.9°C to -2.3°C.

At a scale of 1:15000, the spatial distribution of slush was patchy at Sites 1, 2, and 4, whereas at Site 3 it was extensive. Patchy distributions also corresponded with areas of low slush thicknesses (Table 1). Complete delineation of the actual extent of the slush within, and in the vicinity of, each site was not possible because the slush was concealed beneath the snow cover. However, observations based on the 25 m sampling strategy revealed intra-site isolated slush patches, i.e., alternating patterns of slush and non-slush areas. Mean snow depth varied between sites by up to 6.4 cm, and ice thickness by up to 10.9 cm (Table 1). Site 2 exhibited the greatest variability in both snow depth and ice thickness.

https://doi.org/10.5194/egusphere-2026-4311
Preprint. Discussion started: 23 July 2026

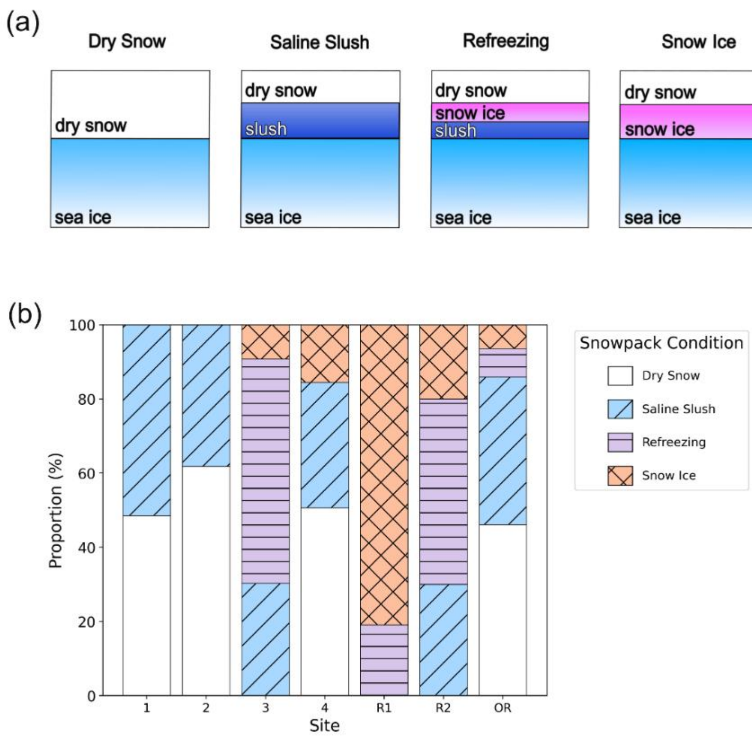

Figure 3: (a) Schematic of the observed snowpack conditions. (b) Proportion of each snowpack condition at each site. R1: Revisit site 1, R2: Revisit site 2, OR: Opportunistic records.

180

Table 1: Ice thickness, snow depth, and slush thickness for each site. Values are in centimeters, and slush thickness includes the snow ice layer at the surface, if present.

		Site			
		1	**2**	**3**	**4**
Snow	Mean	21.5	27.9	23.5	25.8
	Std	5.8	3.6	5.8	4.1
	Min	8.0	16.0	6.0	16.0
	Max	30.0	38.0	34.0	41.0
Ice	Mean	48.2	54.1	50.8	59.1
	Std	5.4	10.8	7.6	4.6
	Min	39.5	28.0	43.0	51.0
	Max	57.5	70.0	73.5	67.0
Slush	Mean	2.0	3.5	10.1	1.0
	Std	3.3	4.5	3.3	2.3
	Min	0.0	0.0	4.0	0.0
	Max	13.0	14.0	22.0	7.0

https://doi.org/10.5194/egusphere-2026-4311
Preprint. Discussion started: 23 July 2026

2.3 SAR Dataset

A total of 23 SAR images were analysed, corresponding to RADARSAT Constellation Mission (RCM), Sentinel-1, and SAOCOM (Table 2). The SAR images are identified by orbit number, or 'Orbit ID', which are typically pairs corresponding to pre- (t_1) and post-flooding (t_2) acquisitions, the latter also coinciding with fieldwork. Exceptions are orbits 67 and 19, which include multiple acquisitions at t_2. Orbit 67 has three acquisitions during fieldwork (67a, 67b, and 67c in Table 2), while orbit 19 has two (19a and 19b in Table 2). Each mission and its acquisitions are further detailed in the following subsections.

SAR images were processed using the European Space Agency's (ESA) Sentinel Application Platform (SNAP) and its Python module Snappy. The general SAR pre-processing steps were calibration to σ^0, speckle filtering, and terrain correction using the ASTER GDEM (1 arc-second resolution). The latter step yielded more accurate geolocation than ellipsoid correction, particularly in mixed land-sea SAR scenes, as it accounts for land topography and improves the positioning of sea ice in channels and along strait margins. For Sentinel-1, the additional steps of orbit correction and thermal noise removal were included, and for IW mode, split and deburst were applied. A multi-look step was applied after calibration to meet square pixels for Single-Look Complex (SLC) products. Across the study area, the incidence angles of the SAR images range from 28° to 55°, and after pre-processing, the image pixel spacings range from 11 to 40 m (Table 2).

2.4.1 RADARSAT Constellation Mission

C-band RCM (5.4 GHz) is operated by the Canadian Space Agency (CSA). A set of 12 images was downloaded from the Earth Observation Data Management System (EODMS) in Ground Range Detected Mode (GRD). The relative orbital numbers for this mission were 119, 67, 104, and 97 (Table 2). Three operational modes make up the RCM image set: Medium Resolution 50m, Low Noise, and Medium Resolution 16m. All images were acquired in linear dual-polarization (HH-HV) mode.

2.4.2 Sentinel-1

ESA operates the C-band Sentinel-1 (5.4 GHz) mission. A set of 8 images was acquired from the Copernicus Data Space Ecosystem using the available modes, Extra-Wide (EW) and Interferometric Wide (IW), and the product types SLC and GRD (Table 2). The orbits corresponding to this mission were 11, 32, 40, and 113. All the images were in linear dual-polarization (HH-HV).

2.4.3 SAOCOM

L-band (1.3 GHz) SAOCOM is an Argentinian mission developed by the Comisión Nacional de Actividades Espaciales (CONAE). CONAE delivered the acquisitions in SLC format. Three SLC-format images were acquired in linear quad-polarization mode (HH-HV-VV-VH), leaving L-band as the only available frequency with VV and VH polarization in the image set. One of the images was acquired before flooding, and the other two were taken after. Orbit 19 corresponds to this mission (Table 2).

https://doi.org/10.5194/egusphere-2026-4311
Preprint. Discussion started: 23 July 2026

2.4.3 SAR Noise Floor

To ensure the quality of SAR data from low return targets such as smooth FYI, the nominal noise-equivalent sigma zero (NESZ), or noise floor, for each acquisition was determined to enable exclusion of data below that threshold. Noise floor values for each swath were extracted from product metadata for Sentinel-1 and RCM. For SAOCOM, the nominal NESZ of −34 dB was used as a reference noise floor (Brunelli & Mancini, 2024). NESZ values were compared to samples acquired from the locations where fieldwork was conducted.

Co-polarization channels did not exhibit values below the noise floor; however, it was considerable for some orbits in the cross-polarization channels (% Noise in Table 2). RCM acquisitions were free of noise values, except for orbit 104, which showed 3% at t_2 and 7% when both times were combined. Sentinel-1 EW acquisitions were increasingly affected by noise at higher incidence angles, with no noisy values for orbit 32 and up to 30-37% for orbits 11 and 40 (Table 2). IW acquisitions (orbit 113) were less affected. SAOCOM cross-polarization data below the noise floor were substantial, particularly when combining acquisitions at t_1 and t_2, which had a stronger impact on change-detection parameters (see Section 2.4). VH showed lower noise values than HV.

Table 2: SAR images in chronological sequence of t_2 where t_1 corresponds to pre-flooding conditions, and t_2 corresponds to post-flooding conditions. IW for Interferometric Wide, EW for Extra Wide, GRD for Ground Range Detected, GRD-M for Ground Range Detected Medium resolution, SLC for Single Look Complex. Dates are in year-month-day format. Incidence angle is the mean incidence angle across fieldwork locations.

Orbit ID	Sensor	Band	Polarization	t_1	t_2	Δ Days	Incidence Angle (°)	Pixel Spacing (m)	Acquisition Mode/Product Type	% Noise t_2 HV (VH)	% Noise t_1 and t_2 HV (VH)
119	RCM	C	HH+HV	2024-04-19	2024-04-27	8	55	20	Medium Resolution 50m/GRD	0	0.4
67 (a)	RCM	C	HH+HV	2024-04-20	2024-04-28	8	44	40	Low Noise/GRD	0	0
11	Sentinel-1	C	HH+HV	2024-04-16	2024-04-28	12	31	40	EW/GRD-M	9	37
32	Sentinel-1	C	HH+HV	2024-04-17	2024-04-29	12	20	40	EW/GRD-M	0	0
19 (a)	SAOCOM	L	Quad-pol	2024-04-14	2024-04-30	16	28	16	Stripmap/SLC	66 (63)	96 (94)
40	Sentinel-1	C	HH+HV	2024-04-18	2024-04-30	12	42	40	EW/GRD-M	17	30
67 (b)	RCM	C	HH+HV	2024-04-20	2024-05-02	12	44	40	Low Noise/GRD	0	0
104	RCM	C	HH+HV	2024-04-22	2024-05-04	12	51	20	Medium Resolution 50m/GRD	3	7
113	Sentinel-1	C	HH+HV	2024-04-23	2024-05-05	12	37	15	IW/SLC and GRD	1	2
67 (c)	RCM	C	HH+HV	2024-04-20	2024-05-06	16	44	40	Low Noise/GRD	0	0
19 (b)	SAOCOM	L	Quad-pol	2024-04-14	2024-05-08	24	28	16	Stripmap/SLC	61 (48)	93 (92)
97	RCM	C	HH+HV	2024-04-14	2024-05-08	24	33	40	Low Noise/GRD	0	0

2.4 SAR Parameters and Feature Generation

Seven SAR parameters were studied: sigma nought (σ^0), co- and cross-polarization ratios (r_{co} and r_{cr}), logarithm ratio (LR), coherence (γ), and texture using the grey-level co-occurrence matrix (GLCM) variance of σ^0 (GLCM Variance) and LR

https://doi.org/10.5194/egusphere-2026-4311
Preprint. Discussion started: 23 July 2026

(GLCM Variance Change) (Table 3). Parameters were categorized into two types for analyses: i) Single-date (SD), and ii) Change Detection (CD) (Table 3). SD involved the analysis of single SAR scenes coinciding with fieldwork and flooding (t_2 in Table 2), while CD considered image pairs acquired before and during flooding from the same orbit (t_1 and t_2 in Table 2). The time differences between CD pairs were 8 to 24 days, depending on the orbit.

r_{co} and r_{cr} ratios, also known as polarimetric discriminators, can provide additional information, and as suggested by Segal et al. (2020b) they should be explored for slush. r_{co} is sensitive to surface conditions and r_{cr} is indicative of volume scattering, with r_{co} approaching zero and r_{cr} increasing when volume scattering increases (Scharien et al., 2012). The r_{co} decreases with increasing surface roughness and decreasing dielectric constant for FYI in C-band (Cafarella et al., 2019; Kim et al., 2012; Nakamura et al., 2006). However, for small-scale ice surface roughness, such smooth FYI, this ratio shows a direct response to the ice surface dielectric constant, with low sensitivity to surface roughness in C-band and negligible sensitivity in L-band (Nakamura et al., 2006).

The r_{cr} has been less studied for smooth FYI, possibly due to low signal-to-noise ratio in the cross-polarization channel (Scharien et al., 2014a; Scheuchl et al., 2004; Wakabayashi et al., 2004), reduced volume scattering due to the shallow penetration depth in FYI (Onstott & Shuchman, 2004), and high variability found in r_{cr} magnitudes (Partington et al., 2010; Scharien et al., 2014b). Nevertheless, this parameter has been found to be useful for ice-water discrimination (Partington et al., 2010), and responds to environmental transitions, such as freezing of ice lids on ponds (Scharien et al., 2014b) at incidence angles lower than 30°.

To better understand the change in backscatter pre- and post-flooding, the LR was chosen, which is widely applied in SAR change detection techniques (Gong et al., 2014; Hou et al., 2014). This parameter provides an easy way to understand whether the backscatter coefficient increases (LR>0), decreases (LR<0), or remains unchanged (LR=0) between consecutive acquisitions, accounting for the statistical properties of SAR images (Rignot & Zyl, 1993). LR has rarely been used in sea ice studies, with only one previous application reported (Gao et al., 2019).

Another SAR parameter relevant to temporal change analysis is γ, which decreases as temporal decorrelation increases, and approaches 1 when the target is stable. Coherence analysis and phase-difference (InSAR) techniques have previously been investigated for sea ice to map the extent and stability of landfast ice (Dammann et al., 2019; Meyer et al., 2011), surface topography (Dierking et al., 2017; Marbouti et al., 2020), and snow thermodynamics and redistribution (Yackel et al., 2026). Although no previous studies have used coherence to detect seawater flooding on sea ice, several studies have applied this parameter for detecting flooding in diverse terrestrial environments (Canisius et al., 2019; Pulvirenti et al., 2016).

Texture information derived from the GLCM matrix can enhance the discrimination and classification of sea ice in SAR images, allowing segmentation of sea ice regions rather than relying only on intrinsic gray levels (Haralick et al., 1973; Maillard et al., 2005; Soh & Tsatsoulis, 1999). During winter and early-melt season, smooth FYI exhibits variability in σ^0 due to changes in basal brine volume driven by snow temperature, salinity, and density variations (Geldsetzer et al., 2009; Mahmud et al., 2020; Yackel et al., 2007), given a relatively fixed rough air-snow interface and dry snow. These variations produce spatial and temporal heterogeneity in neighbouring pixels, which GLCM Variance can quantify. Assuming that flooded areas

https://doi.org/10.5194/egusphere-2026-4311
Preprint. Discussion started: 23 July 2026

affect microwave interactions in a spatially similar manner, possibly reducing heterogeneity among neighboring pixels, this parameter was tested for σ⁰ and LR (Table 3). A kernel size of 100–135 m was applied consistently across the SAR dataset to ensure uniform representation of textural features from images with varying pixel sizes.

SAR parameters were derived for each orbit and polarization, producing 138 SAR features (Table 3). The parameters σ⁰, LR, GLCM Variance, and GLCM Variance Change were calculated for all polarization channels available in the SAR dataset, including HH and HV for C-band and, additionally, VV and VH for L-band. We generated r_{co} using only L-band data, as it was the only dataset with both co-polarization channels available. r_{cr} for the ratio $\frac{HV}{HH}$ was produced for C- and L-band, and the ratio $\frac{VH}{VV}$ for L-band only. Two orbits in our SAR dataset were used to investigate coherence: orbit 113 of C-band Sentinel-1 in IW mode and orbit 19 of L-band SAOCOM. The perpendicular baselines of orbits 113, 19a, and 19b were 145.12 m, 152.58 m, and 480.26 m, respectively, consistent with prior studies (Meyer et al., 2011), as interferometric correlation decreases with increasing perpendicular baseline. Native resolution of each orbit was maintained to assess their detection capabilities.

Table 3: SAR parameters, identified by analysis type, where Single-date (SD) compares the flooded and non-flooded areas in the same SAR scene after the flooding event occurs (t_2), and Change Detection (CD) considers the same areas in image pairs from the same orbit before (t_2) and after flooding (t_2). Formulas and relevant references are also included. N is the number of instances of a given parameter (features) derived from the SAR dataset.

SAR parameter	Analysis type	Formula		Reference	N
Sigma Nought (σ^0)	SD	$\frac{4\pi r^2 P_s}{A_0 P_i}$	P_s: averaged scattered power density P_i: averaged incident power density r: distance between the transmitting system and the target A_0: unit area	Lee and Pottier (2009)	28
GLCM Variance (VAR_{glcm})	SD	$\sum_i^k \sum_j^k (1-\mu)^2 p(i,j)$	μ: average sigma nought value $p(i,j)$: $(i,j)th$ entry in normalized GLCM matrix k: k-pixel window	Haralick et al., (1973)	28
Co-polarization ratio (r_{co})	SD	$\frac{\sigma^0{}_{VV}}{\sigma^0{}_{HH}}$	$\sigma^0{}_{VV}$: Sigma Nought VV polarization channel $\sigma^0{}_{HH}$: Sigma Nought HH polarization channel	(Drinkwater et al., 1992)	2
Cross-polarization ratio (r_{cr})	SD	$\frac{\sigma^0{}_{cr}}{\sigma^0{}_{co}}$	$\sigma^0{}_{cr}$: Sigma Nought of the cross-polarization channel $\sigma^0{}_{co}$: Sigma Nought of the co-polarization channel	(Drinkwater et al., 1992)	14

https://doi.org/10.5194/egusphere-2026-4311
Preprint. Discussion started: 23 July 2026

Logarithm ratio (LR)	CD	$log_{10}\left(\frac{\sigma^0{}_{t2}}{\sigma^0{}_{t1}}\right)$	$\sigma^0{}_{t1}$: Sigma Nought at t_1 $\sigma^0{}_{t2}$: Sigma Nought at t_2	Gong et al. (2014)	28
GLCM Variance change	CD	$VAR_{glcm}(LR)$	VAR_{glcm}: GLCM Variance LR: Logarithm ratio	Haralick et al., (1973) and Gong et al. (2014)	28
Coherence (γ)	CD	$\frac{E[u_{t1}u_{t2}^{*}]}{\sqrt{E[\lvert u_{t1}\rvert^2]E[\lvert u_{t2}\rvert^2]}}$	u_{t1}: complex image at t_1 u_{t2}: complex image at t_2 $E[.]$: expected value *: complex conjugate $\lvert.\rvert$: module	Meyer et al. (2011)	10

2.5 SAR Feature Selection

Samples of SAR parameters were extracted from the field site locations classified as *Flooded* where slush thickness was ≥ 5 cm, and *Non-flooded* where slush was = 0 cm. Observations with slush thicknesses between 0 and 5 cm were excluded to avoid transitional flooding conditions. First, an exploratory analysis of each parameter was performed, and then the relevant statistical features that distinguished the two classes were selected (A in Figure 4). For the exploratory analysis, σ^0 was normalized to an incidence angle of 28°, following Mahmud et al. (2018), to make C-band data comparable with L-band, which ranged from 27.9° to 28.3°. C-band σ^0 HH decreased linearly with incidence angle (−0.23 dB/°; $R^2 = 0.67$), while HV showed a weaker trend (−0.02 dB/°; $R^2 = 0.01$). These values were consistent with previous studies on first-year level ice at C-band (Wiebke et al., 2020).

The two-sample Kolmogorov–Smirnov (KS) test was used to evaluate class separability and for feature selection. The KS test is a nonparametric method that compares two sampled cumulative distribution functions by evaluating the maximum absolute distance between them, without making prior assumptions about the shape of their underlying distributions (Nasonova et al., 2018). The statistical significance and the KS statistic (D) provide information about the separability between two classes. Significance indicates whether samples are likely to come from populations with different distributions (Pratt & Gibbons, 1981) and was assessed using the p-value for a given α (0.05), with $p < \alpha$ indicating significant separation between classes. The KS statistic (D) quantifies the degree of separation, with 0 indicating identical distributions and 1 indicating completely non-overlapping distributions. Features were selected based on higher significant D values, with additional inspection to avoid redundancy and ensure complementary information for the modeling process (Section 2.6).

https://doi.org/10.5194/egusphere-2026-4311
Preprint. Discussion started: 23 July 2026

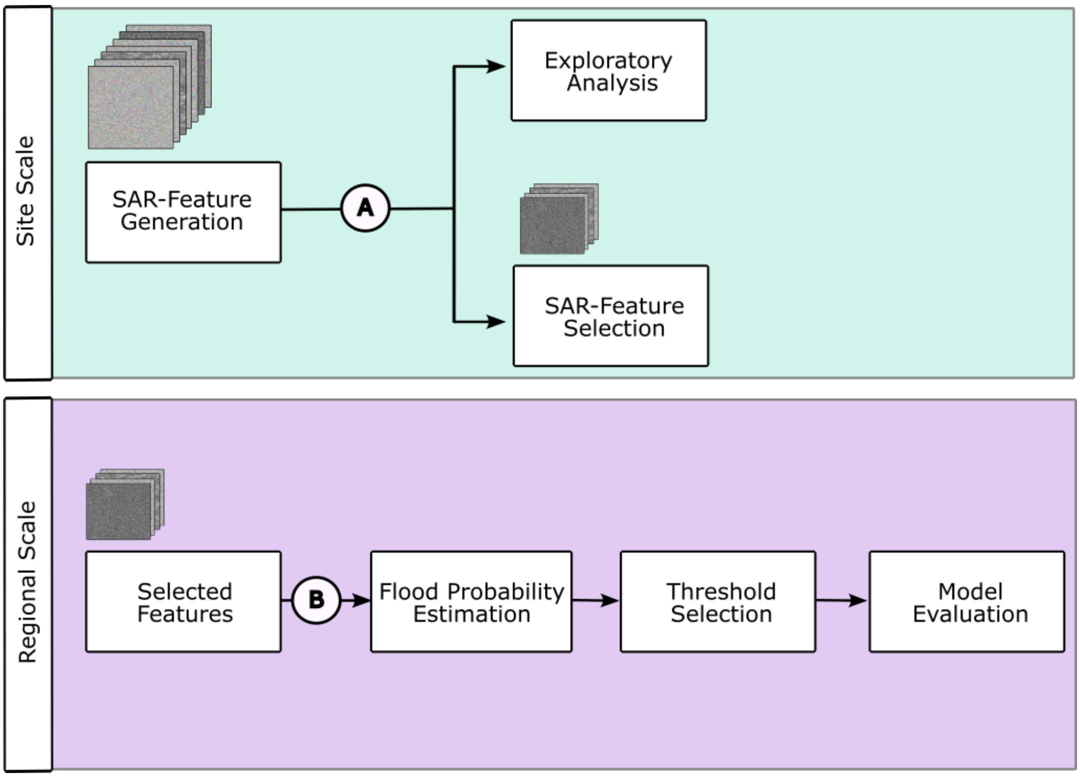

Figure 4: Methodological flow used for SAR-features selection at the site scale, and model development and evaluation at a regional scale.

2.6 Predicting Flooding at a Regional Scale

The selected features were used as input to a Random Forest (RF) classifier to estimate flood probability at a regional scale (Figure 4). To ensure sufficient and balanced data for training and testing *Flooded* and *Non-Flooded* classes, additional randomly selected points from within interpolated areas and from opportunistic records were extracted from the selected features (Step B in Figure 4), both classified using the slush thickness threshold as in Section 2.5.

Interpolation was done on field measurements from Sites 1–4 using Inverse Distance Weighting (Shepard, 1968). IDW was chosen for its simple data requirements and its ability to account for point weights based on proximity to known values, making it a reliable choice for the patchy distribution found in the slush. *Snow ice* observations were excluded from the interpolation due to possible uncertainties of the snow ice–ice interface position. The mean absolute error (MAE) and the root mean square error (RMSE) of the interpolation were 2.2 and 3.5 cm, respectively, as estimated using leave-one-out cross-validation (Risk & James, 2022). One hundred points were randomly distributed within each interpolated area and classified together with the opportunistic records. Points located within 30 m of each other were removed to reduce redundancy in the feature inputs after downscaling for the RF model. The extended points were then split 70–30% for training and testing, stratified by class.

https://doi.org/10.5194/egusphere-2026-4311
Preprint. Discussion started: 23 July 2026

The RF model was trained using the Scikit-learn package in Python (Pedregosa et al., 2011). Model hyperparameters were optimized by systematically testing a small set of possible values and selecting the combination that yielded the best cross-validated performance. The parameters included the maximum depth of each tree, the minimum number of samples required at a leaf node, and the number of trees in the forest. The model outputs the probability of flooding, computed as the average of the trees' predicted class probabilities, where the class probability is the fraction of samples in a leaf that belong to that class.

Model evaluation was performed using two metrics: the area under the receiver operating characteristic (ROC) curve (ROC-AUC) and the F1-Score. ROC-AUC summarizes the predictive performance of a model in separating *Flooded* and *Non-Flooded* classes. ROC curve plots the False Positive Rate (FPR, eq. 1) on the x-axis against the True Positive Rate (TPR, eq. 2) on the y-axis for different probability thresholds. FPR and TPR are obtained from the confusion matrix (Table 4). The ROC-AUC metric allows evaluating model performance across all probability thresholds and is independent of the underlying class imbalance (Richardson et al., 2024). An ROC-AUC score of 0.5 indicates the classifier has no discriminatory ability and is no better than a random classifier; a value of 1 represents a perfect model.

The probability of flooding threshold was later selected using the best F1-Score (eq. 3), calculated using the TPR or Recall (eq. 2), and the Precision (eq. 4). The F1-Score is widely used with an imbalanced dataset representing the harmonic mean of Precision and Recall, balancing the trade-off between when false positives and false negatives are costly (Sujon et al., 2025). F1-Score was calculated at probability thresholds of 0.00, 0.25, 0.50, and 0.75.

Table 4: Confusion Matrix.

		Predicted	
		Positive	Negative
Actual	Positive	True Positive (TP)	False Negative (FN)
	Negative	False Positive (FP)	True Negative (TN)

$$FPR = \frac{FP}{FP + TN} \tag{1}$$

$$TPR = Recall = \frac{TP}{TP + FN} \tag{2}$$

$$F1\ score = 2 * \frac{Precision\ x\ Recall}{Precision +\ Recall} \tag{3}$$

$$Precision = \frac{TP}{TP + FP} \tag{4}$$

https://doi.org/10.5194/egusphere-2026-4311
Preprint. Discussion started: 23 July 2026

3 Results

3.1 Single-Date SAR parameters

HH and HV polarization σ^0 from *Flooded* and *Non-flooded* classes in the t_2 SAR image dataset are shown in Figure 5a and 5b, in chronological order. A change in the HH behaviour was observed on 30 April. Before this date, similar σ^0_{HH} values were found for both classes, whereas, afterward, the *Flooded* class was lower. The mean difference between classes was less than 2.5 dB, though the pattern was persistent and not dependent on incidence angle (Figure 6a). L-band showed the opposite behaviour, on 30 April, where the difference between the mean σ^0_{HH} of *Flooded* and *Non-flooded* classes was positive though *Flooded* and *Non-flooded* overlapped on 8 May.

For σ^0_{HV}, the pattern was less clear in C-band, with the *Flooded* class about 1dB lower in some instances after 30 April, and higher dispersion overall (Figure 5b). Before 30 April, classes were distinguished in C-band only at 20°, corresponding to orbit 32 (Figure 6b, Table 2) and, after 30 April, differences were observed at incidence angles below 37°, except for orbit 67 acquired at 44°. L-band showed almost no difference between classes, neither in σ^0_{HV} (Figure 5b) or in σ^0_{VH} (Figure S1b). Overall, the NESZ and the limited number of samples taken at both C- and L-band are likely to be affecting these results.

The GLCM Variance of σ^0_{HH} revealed differences between classes at C-band, whereas the GLCM Variance of σ^0_{HV} showed differences only in the L-band. At C-band HH polarization, lower heterogeneity was observed for *Flooded* after 30 April (Figure 5c). This difference was mission-dependent, observed only in RCM mission images, and class separability increased with incidence angle (Figure 6c), with the largest difference observed at 51°. For L-band HH and HV polarization GLCM Variance, *Flooded* showed no difference and consistently lower values between the acquisitions, respectively (Figures 5c and 5d).

Differences in the cross-polarization ratio $r_{HV/HH}$ between classes were small, remaining below 1 dB (Figure 5e). For the C-band, the largest differences occurred between 29 April and 4 May, switching from lower values for *Flooded* compared to *Non-flooded*, to the opposite (Figure 5e). On 29 April, $r_{HV/HH}$ was primarily influenced by HV, with differences arising from lower HV backscatter in *Flooded*, since HH backscatter was almost identical for both classes (Figure 5a), whereas on 30 April and 4 May, $r_{HV/HH}$ was driven by HH, with differences arising from lower HH backscatter in Flooded, as HV backscatter was similar between the classes (Figure 5b).

The L-band cross-polarization ratios $r_{HV/HH}$ and $r_{VH/VV}$, as well as the co-polarization ratio $r_{VV/HH}$, showed only differences between classes for the acquisition of 5 May (Figure 5e, 5f, 5g). The limited number of reliable samples influences cross-polarization ratios at this frequency due to the image noise floor.

https://doi.org/10.5194/egusphere-2026-4311
Preprint. Discussion started: 23 July 2026

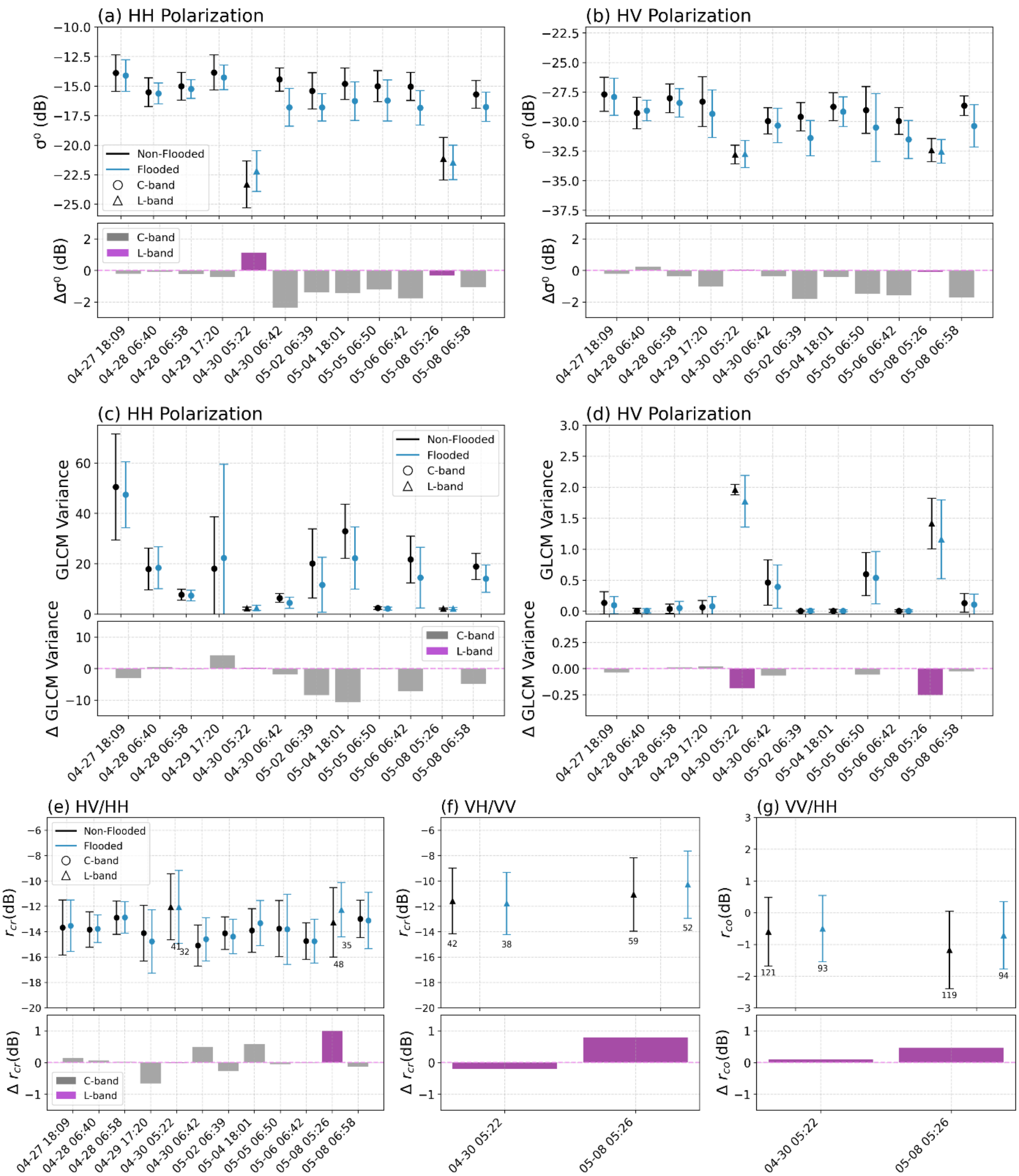

Figure 5. Single-date SAR parameters for C- and L-band for *Flooded* and *Non-flooded* classes (top) and mean difference between *Flooded* and *Non-flooded* classes (bottom) for: (a) σ^0_{HH} and (b) σ^0_{HV} normalized σ° at 28° of incidence angle, (c) $GLCM\ Variance_{HH}$ (d) $GLCM\ Variance_{HV}$, Cross-polarization ratio of (e) $r_{HV/HH}$ and (f) $r_{HV/VV}$, and Co-polarization ratio ($r_{VV/HH}$). Error bars represent mean ± 1 standard deviation. For GLCM Variance, skewed distributions may cause the lower bound of the standard deviation to fall below zero. Number labels in the plot indicate the number of records plotted for the L-band. Date and time are given in local time.

https://doi.org/10.5194/egusphere-2026-4311
Preprint. Discussion started: 23 July 2026

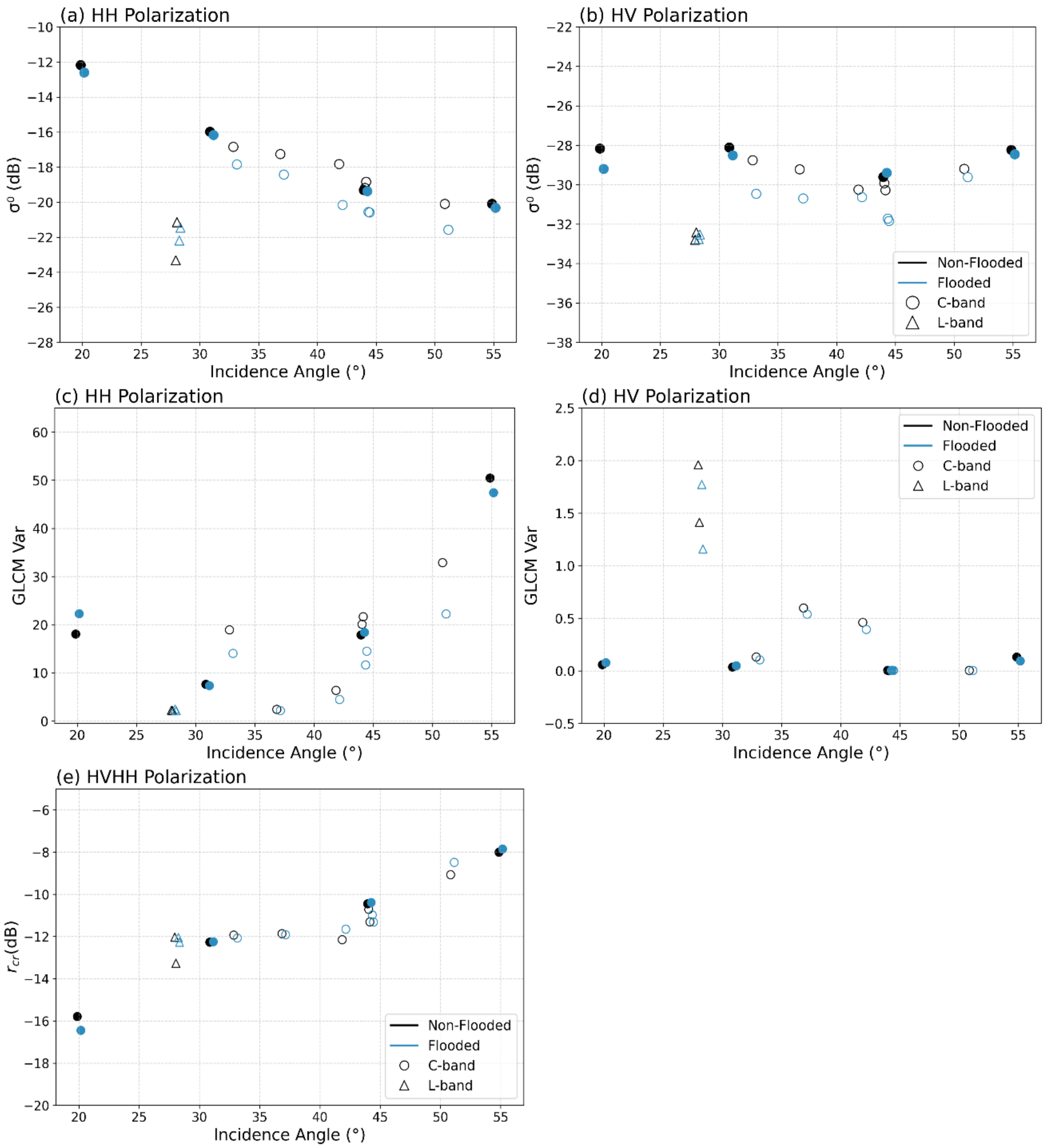

Figure 6. Single Date SAR parameters and incidence angle for C- (circles) and L-band (triangles) for *Non-flooded* (black) and *Flooded* (blue) classes for: (a) σ^0_{HH} and (b) σ^0_{HV} normalized σ⁰, (c) $GLCM\ Variance_{HH}$ (d) $GLCM\ Variance_{HV}$, and the cross-polarization ratio of (e) $r_{HV/HH}$. Filled symbols represent dates before 30 April.

3.2 Change Detection SAR parameters

The LR of acquisitions from t_1 and t_2 for each orbit is presented in Figure 7a for HH polarization and Figure 7b for HV polarization, with the x-axis showing the t_2 acquisition date. L-band cross-polarization channels are presented but not analyzed due to the limited number of records, caused by the influence of the NESZ in both t_1 and t_2 acquisitions (Figure 7b, Table 2).

As noted for σ^0 (Section 3.1), from 30 April, a decrease in *Flooded* HH backscatter was consistently observed ($LR_{HH} < 0$), allowing differentiation (Figure 7a). The C-band LR_{HV} showed a consistent difference starting from 29 April, with the highest difference on 29 April (Figure 7b) corresponding to the smallest 20° incidence angle (Figure 8b). In L-band, LR_{HH} and LR_{VV} were consistently positive, with the increase in backscatter greater for the *Non-flooded* class, indicating distinction between classes (Figure 7a, Figure S2). The distinction increased over time, as reflected by higher LR values on 8 May.

The GLCM variance of LR, or GLCM variance change, showed a wider range of values than when applied to single-scene σ^0 (Section 3.1), indicating greater spatial variability. From 29 April, both C- and L-band acquisitions showed greater homogeneity in the *Flooded* class at HH polarization (Figure 7c), with lower values than the *Non-flooded* class. Higher HH GLCM variance change values were also observed in the C-band acquisitions on 29 and 30 April for both classes, indicating greater heterogeneity. This effect is also visible in Figure 8c at incidence angles of 20° and 42°, corresponding to those dates (Figure 8c). The dependence of this parameter on incidence angle was less sensitive than when applied to σ^0 (Figure 6c, 8c). *Flooded* areas were also more homogeneous after 29 April in the C-band GLCM variance change for HV polarization. Of note, the largest differences correspond to better imaging conditions in terms of the NESZ. On 29 April, orbit 32 was acquired at a steep 20° incidence angle, promoting stronger signal returns, and images on 2, 6, and 8 May were acquired by RCM operating in Low Noise mode (Figures 7d, 8d).

Regarding γ, differences between classes were observed only in L-band co-polarization channels (Figure 7e–h). L-band γ_{HH} and γ_{VV} of the *Non-flooded* class showed higher coherence, with average values above 0.35, indicating less temporal phase decorrelation than the *Flooded* class. Differences between classes were larger when the time difference between t_1 and t_2 acquisitions was smaller, as observed for orbit 19a with a 16-day interval (29 April) compared to orbit 19b with a 24-day interval (8 May).

https://doi.org/10.5194/egusphere-2026-4311
Preprint. Discussion started: 23 July 2026

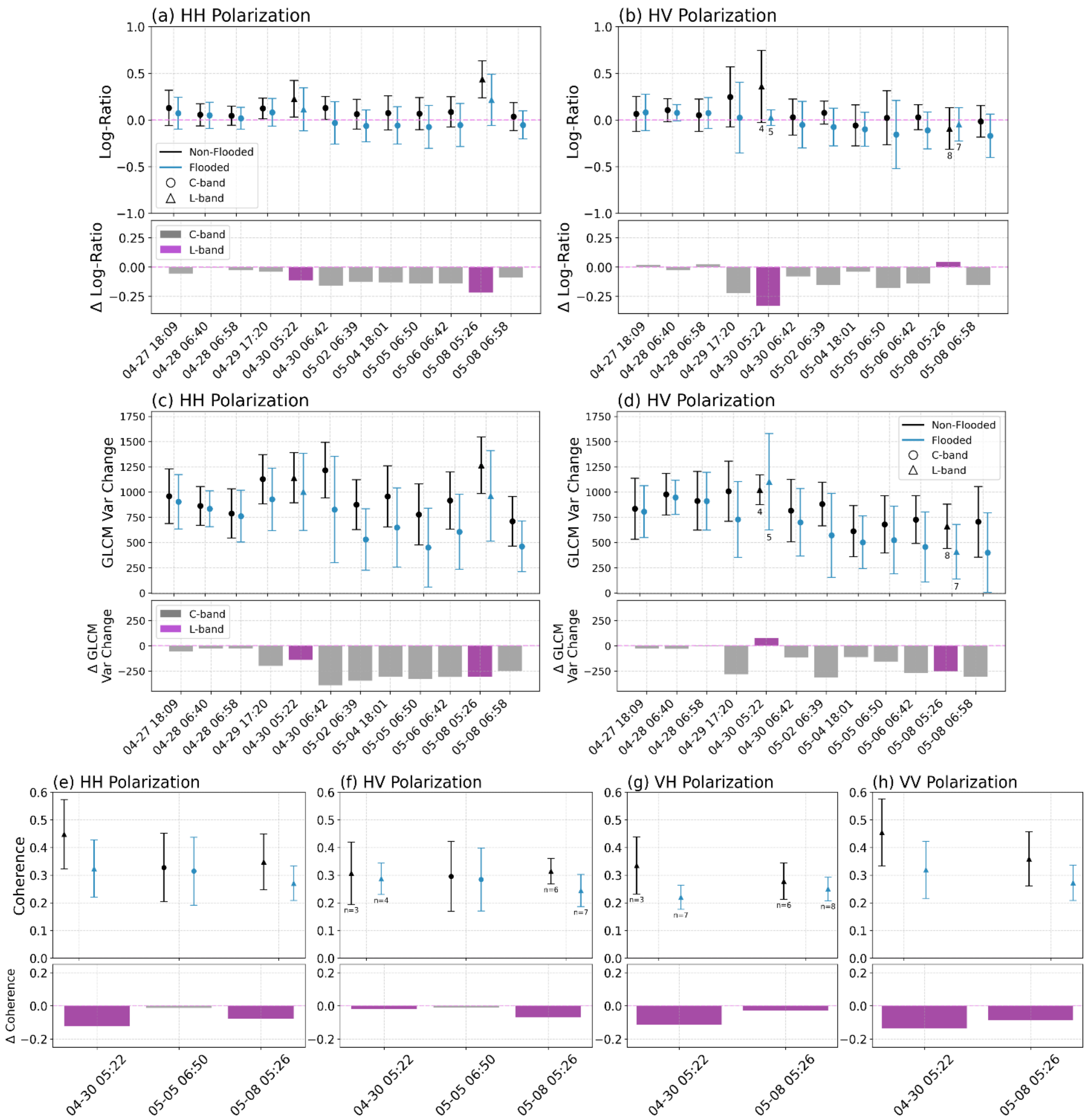

Figure 7. Change detection SAR parameters for C- and L-band for *Flooded* and *Non-flooded* classes (top) and mean difference between *Flooded* and *Non-flooded* classes (bottom) for: Logarithm ratio (LR) (a) HH and (b) HV polarizations, GLCM Variance Change (c) HH and (d) HV polarizations, and coherence (γ) for (e) HH, (f) HV, (g) VH and (h) VV polarizations. Error bars represent mean ± 1 standard deviation. Number labels in the plot indicate the number of records plotted for the L-band. Date and time are given in local time, and the x-axis shows the t2 acquisition date of the image pair.

https://doi.org/10.5194/egusphere-2026-4311
Preprint. Discussion started: 23 July 2026

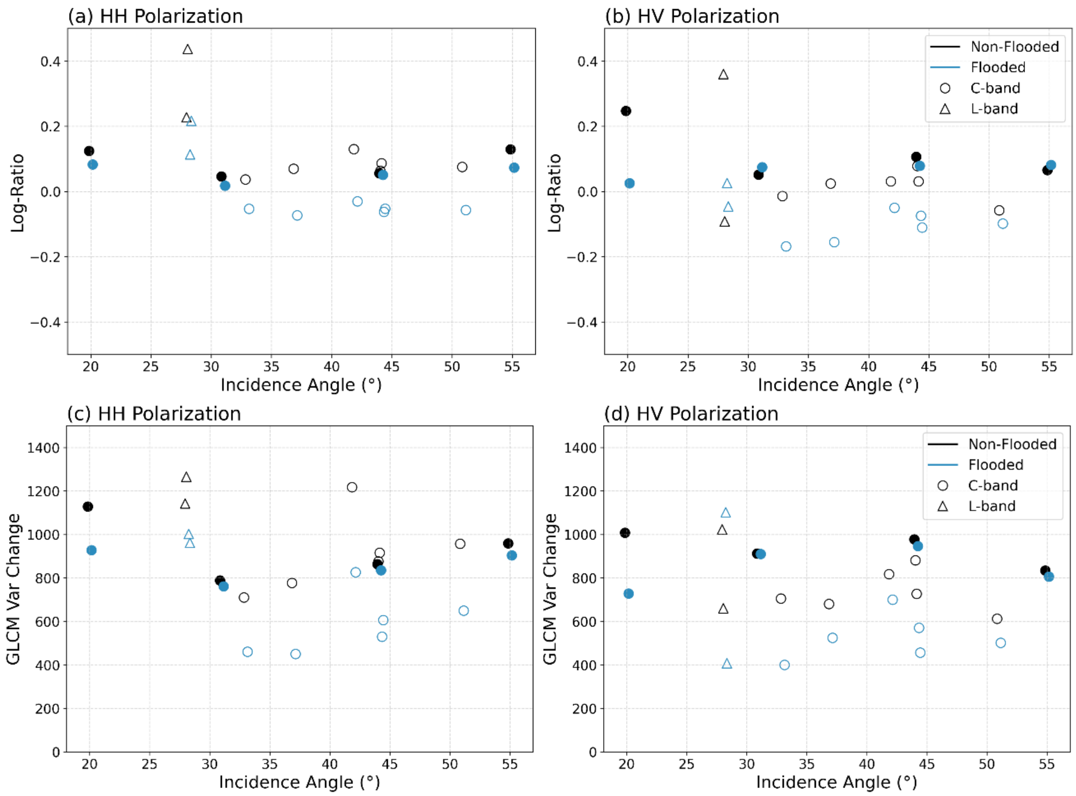

Figure 8. Change detection SAR parameters and incidence angle for C- (circles) and L-band (triangles) for *Non-flooded* (black) and *Flooded* (sky-blue) classes for: Logarithm ratio (LR) (a) HH and (b) HV polarizations, GLCM Variance Change (c) HH and (d) HV polarizations. Filled symbols represent dates of t_2 images before 30 April.

3.3 Sensitivity of SAR-derived Parameters to Surface Flooding

The KS statistic D showed that γ provided the largest separation between *Flooded* and *Non-Flooded* classes, with L-band γ_{HH} and γ_{VV} $D \geq 0.5$ (Figure 9a, 9b). This was followed by GLCM Variance Change, where class separation exhibited a time-dependent behavior, starting around orbit 32 (29 April) and increasing over time (Figure 9c). Three instances of this parameter showed strong separability, with $D \geq 0.5$: C-band orbits 113 and 97 in HH polarization, and L-band orbit 19b in both co-polarized channels, all corresponding to dates after 5 May.

Textural information appeared to enhance class separability, showing a consistent pattern for orbits following 29–30 April. This is supported by higher KS statistic values in Figure 9 when comparing GLCM Variance Change (9c) and GLCM Variance (9e) with the SAR parameter from which they were derived (9d and 9f, respectively). Overall, change detection parameters and co-polarization channels demonstrated the greatest effectiveness in distinguishing classes. The KS test for γ was not statistically significant for C-band, indicating that the γ distributions overlapped substantially.

https://doi.org/10.5194/egusphere-2026-4311
Preprint. Discussion started: 23 July 2026

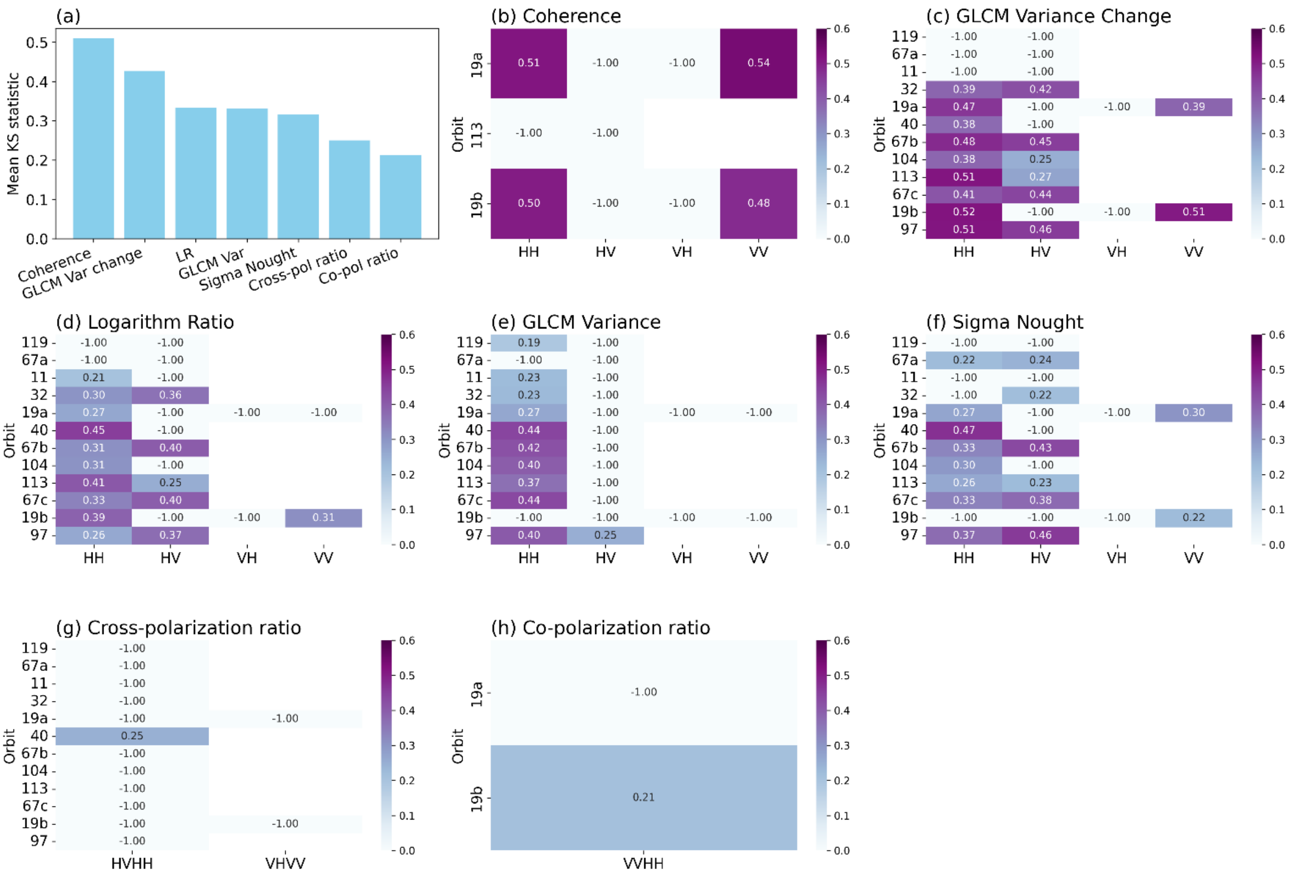

Figure 9. (a) SAR parameters and their mean KS statistic. (b–h) SAR parameters are shown by orbit ID, chronologically ordered in descending order of t^2, and by polarization. The KS statistic (D) is displayed as a number for each feature, along with a color scale. A KS value of –1.00 indicates a non-significant test at $\alpha = 0.05$.

The seven features exhibiting the highest KS statistics ($D \geq 0.5$) are shown in Figure 10, ordered by decreasing D value. These seven features shared similar spatial patterns. The L-band co-polarized γ features captured the same information (Figure 10a, 10d, 10g). L-band GLCM variance change showed clear qualitative distinctions from γ (Figure 10b), with no noticeable differences between the two co-polarization channels (Figure 10b, 10f). However, this textural feature showed stronger differences between L- and C-band (Figure 10c, 10e).

Selection of features was based on the highest D values while avoiding redundancy among variables, resulting in a set of three features (IDs 1–3). The first two capture distinct L-band information: phase decorrelation (Feature ID 1) and textural information of backscatter change (Feature ID 2). Feature ID 3 adds information on backscatter change at a complementary frequency, C-band. Overall, this feature set offers enhanced discrimination while minimizing redundancy in subsequent model inputs.

https://doi.org/10.5194/egusphere-2026-4311
Preprint. Discussion started: 23 July 2026

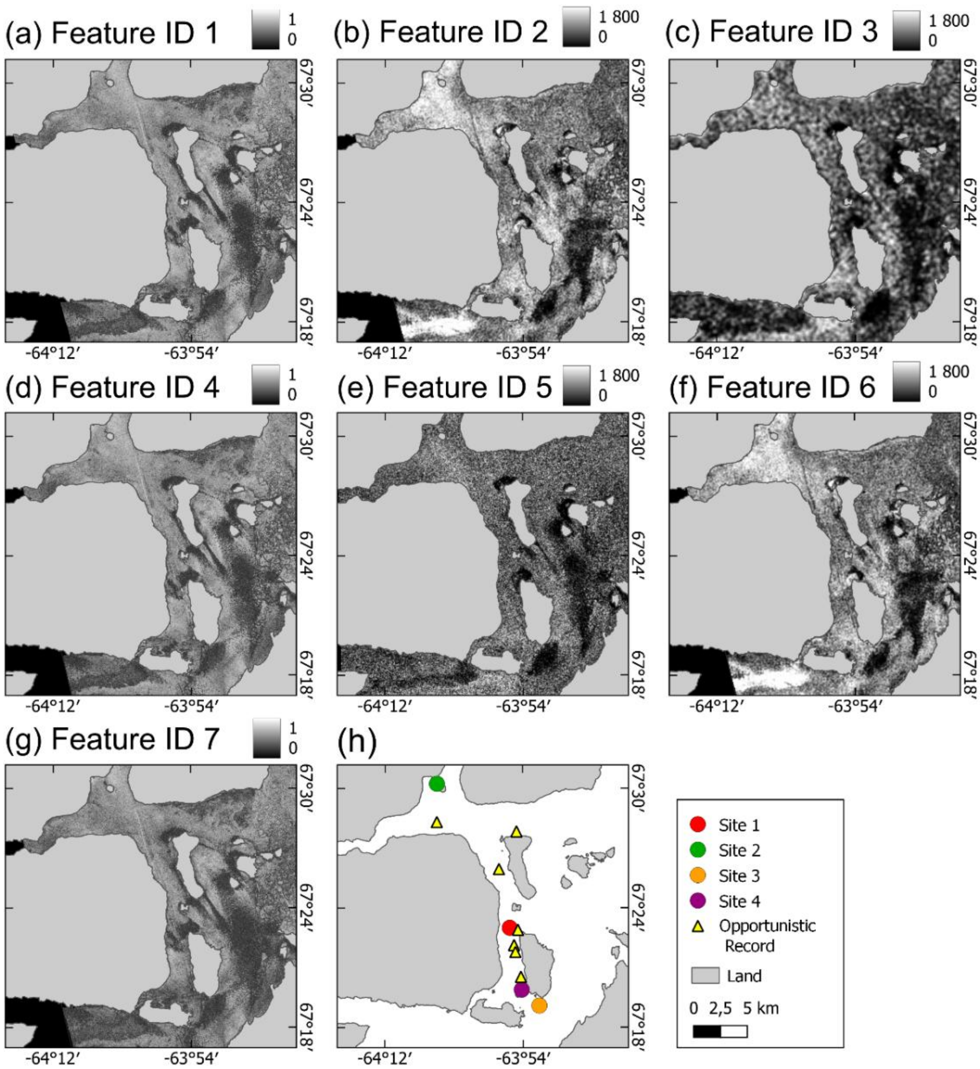

Figure 10. Features with a Kolmogorov–Smirnov statistic D ≥ 0.5, shown by feature ID (1–7) in panels (a–g). (h) Overview of the study area showing sites (points) and opportunistic records (triangles). Background imagery: (a, b, d, f and g) SAOCOM® Product – ©CONAE 2024. All Rights Reserved; (c) RADARSAT Constellation Mission imagery © Government of Canada (2024). RADARSAT is an official mark of the Canadian Space Agency; (e) Copernicus Sentinel data 2024.

3.4 Retrieval at the Regional Scale

Three approaches were used to estimate the probability of flooding: (1) a RF model including Feature IDs 1 and 2; (2) a RF model including Feature IDs 1- 3; and (3) a simple threshold of 1 − Coherence derived from the VV coherence of orbit 19a (Table 5). Since flooded areas exhibited lower coherence values, using 1 − Coherence provided a measure comparable to the probability of flooding.

https://doi.org/10.5194/egusphere-2026-4311
Preprint. Discussion started: 23 July 2026

1 − Coherence achieved an ROC-AUC of 0.85, indicating that this feature alone already provides substantial capability to distinguish between the two classes. Including additional features further improved performance, with ROC-AUC values of 0.88 for Model 1 and 0.90 for Model 2. The F1-score for each flooding probability in distinguishing between the two classes is shown in Table 6. The best threshold was obtained at a probability of flooding of 0.50 across all cases. Separating classes with a probability of 0.50 gave an F1-score of 0.81 for 1-coherence, 0.85 for Model 1, and 0.87 for Model 2.

Table 5. Input features used in each model. Features indicate feature ID, SAR parameter, sensor, orbit ID, and polarization.

Model	Input Feature
1-Coherence	ID1–Coherence–SAOCOM–19a–VV
1	ID1–Coherence–SAOCOM–19a–VV ID2- GLCM Variance Change–SAOCOM–19b–HH
2	ID1–Coherence–SAOCOM–19a–VV ID2–GLCM Variance Change–SAOCOM–19b–HH ID3–GLCM Variance Change –RCM–97–HH

Table 6. F1 scores corresponding to different thresholds for 1-Coherence and the Random Forest models 1 and 2.

	Probability of Flooding	1-Coherence	Model 1	Model 2
Threshold	0.00	0.00	0.78	0.78
	0.25	0.63	0.83	0.80
	0.50	0.81	0.85	0.87
	0.75	0.78	0.81	0.81

Predictions applied to entire SAR scenes, which broadly cover the study area, provided qualitative insights into the spatial patterns of flooding. Consistent with the evaluation metrics, increasing the number of features led to better delineation of flooded and non-flooded areas (Figure 11b-c). Given the limited validation data outside the surveyed sites and from opportunistic records, the locations of subsequently formed polynyas were considered as subjective indicators of thinner sea ice and earlier flooding events due to snow loading. The later-formed polynyas were identified in an 11 June Sentinel-2 image, 35 days after fieldwork (Figure 11a).

All polynyas developed in areas where the three models consistently identified a high probability of flooding (Figure 11a-11d). Sites 1 and 3 were located 390 m west and 148 m south, respectively, of the polynyas, while a polynya developed directly at Site 2. Extensive areas to the east of Site 1 and north of Site 3 were identified as flooded in all three models (Figure 11b-11d). At east of Site 1, thin sea ice containing 4 cm of slush was measured as opportunistic records, validating that area.

When comparing the models, both discrepancies and similarities are observed in specific areas, namely Zones 1 (Z1), 2 (Z2), and 3 (Z3) (Figure 11a). In Z1, 1-Coherence indicates flooding, whereas Models 1 and 2 do not. According to the community, slush is not recurrent in this area (Ikirmiut Community Management Committee, 2023), suggesting a possible overestimation when using coherence alone. Including C-band information improves the identification of this area as non-flooded, as observed when moving from Model 1 to 2.

https://doi.org/10.5194/egusphere-2026-4311
Preprint. Discussion started: 23 July 2026

At Z2, all models recognized a high probability of flooding, with the highest probability found near the polynyas observed between Baffin and Qikiqtaq islands (Figure 11a). The community recognizes part of this area and regions further west of Z2 as current slush areas, although model validation remains limited. This area showed contrasting GLCM variance changes between L- and C-band, with high heterogeneity in L-band (Figure 10b, 10f) but not in C-band (Figure 10c, 10e), potentially indicating sensitivity to slush properties not represented in the sampled sites. This also suggests that combining both frequencies could provide a valuable complement.

Additionally, Z3 showed a flooding area with a north-south pattern direction in all three models. When observing the breakup evolution of the landfast ice from 6 June to 11 July, on 9 July, all the areas at Z2 and Z3 broke up first, possibly indicating a thinner or more fragile surface in these zones (Time-lapse S1 in Supplement Material). The north-south pattern at Z3 aligns with the ice edge east of Z3; however, no other information in the auxiliary data can be used to validate the results.

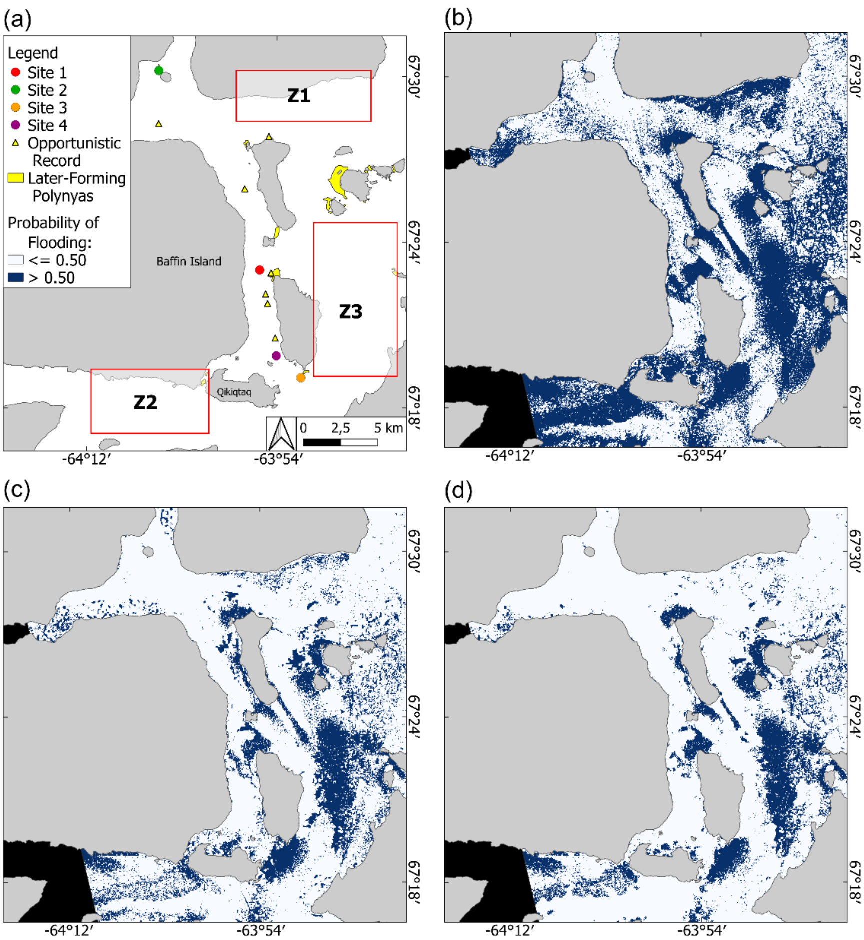

Figure 11. (a) Overview of the study area indicating sites (points), opportunistic records (triangles), and later-formed polynyas (yellow polygons). Zone 1: Z1, Zone 2: Z2, Zone 3: Z3. Predicted probability of flooding using the (b) 1-Coherence, (c) model 1, and the (d) model 2. Black areas correspond to no-data regions beyond the SAR scene coverage.

https://doi.org/10.5194/egusphere-2026-4311
Preprint. Discussion started: 23 July 2026

4 Discussion

4.1 Coherence for Detecting Seawater Flooding

The L-band co-polarization γ parameter showed the strongest association with flooding, suggesting this feature is suitable for flooding detection. *Flooded* class exhibited lower γ values than *Non-flooded* due to surface changes between acquisitions. A cold, non-flooded, landfast FYI surface will primarily backscatter the L-band signal from the ice surface, with secondary contribution from the ice volume, remaining stable from pre-flooding (t_1) to post-flooding (t_2). Snow loading or ice thinning can reduce freeboard, promoting flooding and basal slush formation, and creating a high-dielectric interface at a new height relative to the satellite (Figure 12). This change enhances phase decorrelation and reduces the γ between the two images.

In flooded areas, upward capillary action of seawater through the snowpack could increase the liquid water content in the snow (Mallett et al., 2024), favoring volume scattering. Phase decorrelation due to volume scattering could also reduce the γ in flooded areas and, in C-band, even in non-flooded ones. In C-band, changes in snow volume across successive passes might be reducing γ during the period analyzed, due to the higher sensitivity of C-band to the overlying snow cover than L-band in the early-melt season, with top-of-snow temperatures observed to reach values above -5°C on the day of Sentinel-1 IW acquisition. Even though L-band generally performs well until the advanced melt onset season (Karlsen et al., 2024; Mahmud et al., 2020), further studies are needed to evaluate this limitation at this frequency.

Higher temporal and perpendicular baselines led to greater γ loss. For SAOCOM, performance remained acceptable for L-band up to 24 days between pre- and post-flood acquisitions and perpendicular baselines up to 480 m. The highest separability was observed for orbit 19a, which had a shorter temporal baseline of 16 days and a smaller perpendicular baseline of 153 m, compared to orbit 19b, which had a 24-day temporal baseline and a 480 m perpendicular baseline. The γ values over non-flooded landfast ice were higher than those reported by Meyer et al. (2011), possibly due to the higher temporal and perpendicular baselines (46 days and 570-910 m respectively) in that study. However, γ loss can be associated with other changes in the ice, such as movement or deformation processes (Dammann et al., 2019; Meyer et al., 2011), or with changes in snow properties, such as basal snow brine volume (Yackel et al., 2026). Additional interpretation is required to predict flooding using this parameter alone. The effects of temporal and perpendicular baselines warrant further investigation but are beyond the scope of this study.

https://doi.org/10.5194/egusphere-2026-4311
Preprint. Discussion started: 23 July 2026

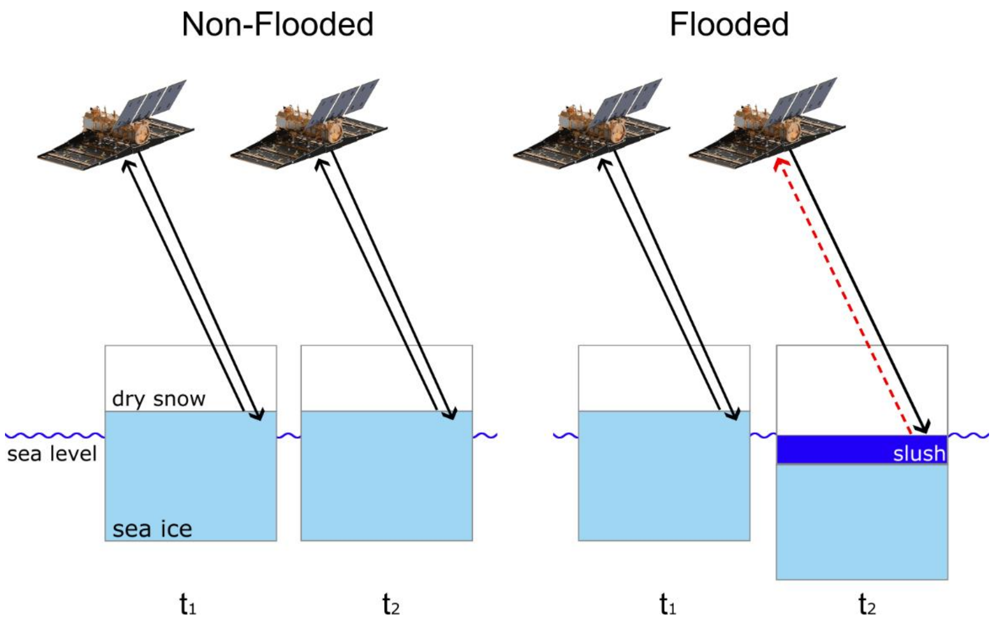

Figure 12. Conceptual diagram illustrating the loss of coherence (γ) in seawater flooded areas in L-band. When comparing acquisitions from time 1 (pre-flooding) and time 2 (post-flooding), areas with a saline slush layer decorrelate the signal, reducing the similarity between the image pair. In contrast, the phase contributions of non-flooded sea ice surface remain stable. The flooded condition represents a scenario in which heavy snow loads push the ice below the seawater level.

4.2 Slush and snow ice formation

The period around 29-30 April provides an opportunity to examine the formation of snow ice and its effect on backscatter. The decrease in snow temperature below -15°C on 29 April, together with the clear-sky conditions on 30 April, promoted the formation of snow ice. At C-band, no differences were observed between the *Flooded* and *Non-Flooded* classes for σ^0_{HH} and LR_{HH} prior to 30 April. In contrast, marked changes were observed after 30 April. The refreezing of slush was reflected in consistently lower σ^0_{HH} values and negative LR values for the *Flooded* class compared to the *Non-flooded* class, while the *Non-flooded* class remained relatively stable. This decrease, attributed to a reduction in the dielectric constant during snow–ice formation, has been reported in the literature to be associated with decreased liquid water content and salinity (Drinkwater & Lytle, 1997).

The GLCM Variance, applied both to σ^0 and LR, improved the ability to distinguish snow ice. *Flooded* class exhibited less spatial heterogeneity at scales of 100 to 135 m than *Non-flooded* when snow ice formed. Prior to 29 April, both classes exhibited similar texture. Our findings support the potential monitoring snow ice formation using time series GLCM Variance Change, from C-band HH polarization, for example by integrating Sentinel-1 and RCM C-band missions. Co-polarization channels are superior for separating classes compared to cross-polarization. For cross-polarization, the HV channel from the Low Noise mode of RCM was superior to Sentinel-1, and smaller incidence angles were more favorable for detection,

https://doi.org/10.5194/egusphere-2026-4311
Preprint. Discussion started: 23 July 2026

producing stronger returns. The advantages of RCM Low Noise mode for cross-polarization channels over smooth FYI were recently reported (Macdonald et al., 2024), and the results from this work corroborate these findings.

L-band σ^0 and LR exhibited distinct between-class behavior during wet slush conditions, reflecting the dielectric contrast between *Non-Flooded* and *Flooded* areas and its greater penetration into *Non-Flooded* areas compared to C-band. When comparing the two L-band acquisitions on 30 April and 8 May, backscatter from *Non-flooded* areas increased while the *Flooded* class remained relatively stable despite slush refreezing into snow-ice. Since the roughness of *Non-flooded* areas did not change, the increase is likely due to the increase in dielectric constant due to seasonal warming, perhaps combined with volume scattering from enhanced brine channels and voids within the ice, detectable by L-band due to its higher penetration. Ice core data also support this interpretation, showing well-developed vertical drainage channels. The lack of sensitivity to snow ice formation across the two examined scenes, as well as higher σ^0 values in slush conditions, requires further analysis with additional input scenes.

4.2 Seawater flooding at a regional scale

Predicting the probability of flooding at a regional scale was possible using L-band γ, and better performance was obtained by incorporating C- and L-band texture information. Later-formed polynyas proved useful for indirectly validating the models; however, in situ confirmation for locations not visited remains unknown. Confirming slush presence is challenging, given its location beneath the snow layer and the limited understanding of how flooded areas are spatially distributed.

Records of flooding have generally focused on reporting the events and providing profile information (Ackley et al., 2020; Geilfus et al., 2023; Haas et al., 2001; Hosseinmostafa et al., 1995; Hoyland, 2009); however, little attention has been given to their spatial dimension. In Arctic lakes, Gusmeroli and Grosse (2012) used ground-penetrating radar to determine the extent of slush and the intensity of overflow. They observed extensive overflow, with freshwater slush extending up to 175 m. In Antarctica, Arndt et al. (2017) surveyed a FYI floe using an electromagnetic induction instrument, finding that flooding occurred in areas smaller than 100 m^2. We found flooded areas extending up to 0.22 km^2, as observed at site 3, and even areas with patches of slush covering approximately 320 m^2.

Remote sensing technologies such as electromagnetic induction can provide a solution (Arndt et al., 2017; Neudert et al., 2025), yet regional validation remains a challenge, and improvements in SAR input models may help address this limitation. Additionally, traditional community knowledge can serve as an indirect validation dataset providing potential solutions, such as SmartICE's Inuit Qaujimajatuqangit Sea-Ice Travel maps that highlight recurrent *massak* zones (Ikirmiut Community Management Committee, 2023; Wilson et al., 2021).

5 Conclusions

This study determined the sensitivity of C- and L-band SAR to seawater flooding and slush and snow ice occurrence on late winter, pre-melt Arctic first-year ice (FYI), with the aim of supporting safer ice travel in communities vulnerable to ice

https://doi.org/10.5194/egusphere-2026-4311
Preprint. Discussion started: 23 July 2026

flooding. Seven SAR parameters were studied: sigma nought (σ^0), co- and cross-polarization ratios (r_{co} and r_{cr}), logarithm ratio (LR), coherence (γ), and texture using the grey-level co-occurrence matrix (GLCM) variance of σ^0 (GLCM Variance) and LR (GLCM Variance Change).

Our findings demonstrate that multi-frequency SAR features provide valuable information for observing surface flooding and, specifically, detecting slush and snow ice phases independently. L-band γ is the most sensitive feature for distinguishing *Flooded* from *Non-flooded* classes while σ^0 and LR are influenced by the state of the slush, decreasing in magnitude as snow ice formation occurred. The low separability of σ^0 and LR between classes under liquid slush conditions indicates that the microwave backscatter of the snow-slush-ice medium depends on multiple interacting factors within the snowpack rather than solely on dielectric property contrasts.

When estimating the probability of seawater flooding at the regional scale, L-band γ alone proved effective. Even though we found stable γ for non-flooded areas in pre-melt conditions with a temporal baseline of up to 24 days, the seasonal evolution and the role of snow in microwave interactions with the ice surface must be further characterized. Larger datasets are needed to better understand other potential processes contributing to γ loss over FYI and under different flooding conditions.

Incorporating GLCM Variance Change when snow ice formation takes place improved overall flooding occurrence estimations. This was observed with coherence, achieving an F1-score of 0.81, increasing to 0.85 and 0.87 in the random forest models including GLCM Variance Change of L-band and C- and L-band together. Texture information from σ^0 and LR proved useful for detecting snow ice, especially in HH polarization, due to increased homogeneity in flooded areas during refreezing. The results demonstrate the potential of time-series GLCM Variance from C-band HH polarization for monitoring snow ice formation, which could even be enhanced by integrating multiple C-band SAR missions such as Sentinel-1 and RCM.

Challenges remain in fully resolving the spatial and temporal variability of snow and slush properties and their impacts on the SAR signal, particularly regarding validation across the SAR scene. Detecting slush thinner than 5 cm, understanding re-freezing dynamics, and characterizing slush spatial distributions remain difficult. The hidden nature of slush, beneath the snow layer, limits characterization of its true spatial distribution, and validation of the entire SAR scene remains unresolved. The use of indirect datasets, such as polynyas, and traditional community knowledge proved useful for understanding the nature of slush, its manifestation in SAR imagery, and its influence on sea ice evolution.

Finally, these results demonstrate the potential of SAR to support the detection and monitoring of saline slush, providing information that could contribute to safer community ice travel. The proposed approach shows promise for identifying slush conditions along commonly used travel corridors at regional scales, with spatial resolutions of less than 50 m, and could support near-real-time or weekly updates of seawater flooding maps. SAR-derived metrics, such as γ, have the potential to be automated and incorporated into operational travel safety maps. Integrating these sources of knowledge could further improve the interpretation and application of SAR-based slush mapping. Such advancements will contribute to a better understanding of sea ice processes, with relevance for both scientific research and local communities.

https://doi.org/10.5194/egusphere-2026-4311
Preprint. Discussion started: 23 July 2026

Code availability

The code is accessible on demand.

Data availability

The RCM data were provided by the Government of Canada subject to the RADARSAT Constellation Mission (RCM) - Public User License Agreement. RADARSAT Constellation Mission Imagery © Government of Canada (2024). RADARSAT is an official mark of the Canadian Space Agency. The SAOCOM data were provided by SAOCOM® product – © CONAE – 2024 All Rights Reserved. Sentinel-1 data was provided by Copernicus Sentinel data 2024.

Author contribution

CSS, RKS and SH conceived and designed the analysis; CSS, RKS, DI, RB collected fieldwork data; CSS, RKS, DI, RB, TB and SH contributed to the methodology and analysis; RKS and SH supervised the study; CSS performed the data processing and analysis; CSS, RKS, RB, TB and SH contributed to writing, reviewing, and editing.

Competing interests

The authors declare that they have no conflict of interest.

Acknowledgements

The authors respectfully acknowledge the Qikiqtarjuaq community and Inuit Nunangat for welcoming us onto their land and participating in or otherwise supporting this study. Special thanks go to Mara Neudert and Carl Thibault for their support in field data collection. We thank the Comisión Nacional de Actividades Espaciales (CONAE), including Marisol Arellano and Pablo Daniel Pepe, for providing the SAOCOM® product – © CONAE – 2024 All Rights Reserved – and for technical support. Finally, we are grateful to Monique Bernier for sharing her valuable experience, which strengthened this research. Additionally, we acknowledge the use of OpenAI's ChatGPT to review the spelling and grammar of portions of an earlier version of this manuscript.

Financial Support

Funding for this research was provided by The Canada-Inuit Nunangat-United Kingdom Arctic Research Programme (CINUK; DOI: https://doi.org/10.69777/323440) grants to authors S. Homayouni and T. Bell, the Canadian Space Agency (24AO3INRS5) grant to S. Homayouni, a New Frontiers in Research Fund – International (NFRF-I) grant to R. Scharien and T. Bell (207-2023-2024-Q4-00667), and a Natural Sciences and Engineering Research Council of Canada (grant no. 110_2022_2023_Q1_2082) to R. Scharien. The authors also gratefully acknowledge the support of the University of Sherbrooke's NSERC CREATE program, De l'Observation de la Terre aux Services d'information décisionnelle (DOTS).

References

Ackley, S. F., Perovich, D. K., Maksym, T., Weissling, B., & Xie, H. (2020). Surface flooding of Antarctic summer sea ice [Article]. *Annals of Glaciology*, *61*(82), 117-126. https://doi.org/10.1017/aog.2020.22

Arndt, S., Meiners, K. M., Ricker, R., Krumpen, T., Katlein, C., & Nicolaus, M. (2017). Influence of snow depth and surface flooding on light transmission through Antarctic pack ice [Article]. *Journal of Geophysical Research-Oceans*, *122*(3), 2108-2119. https://doi.org/10.1002/2016JC012325

Barber, D. G., & Nghiem, S. V. (1999). The role of snow on the thermal dependence of microwave backscatter over sea ice. *Journal of Geophysical Research: Oceans*, *104*(C11), 25789-25803. https://doi.org/https://doi.org/10.1029/1999JC900181

Brunelli, B., & Mancini, F. (2024). Comparative analysis of SAOCOM and Sentinel-1 data for surface soil moisture retrieval using a change detection method in a semiarid region (Douro River's basin, Spain). *International Journal of Applied Earth Observation and Geoinformation*, *129*, 103874. https://doi.org/https://doi.org/10.1016/j.jag.2024.103874

Cafarella, S. M., Scharien, R., Geldsetzer, T., Howell, S., Haas, C., Segal, R., & Nasonova, S. (2019). Estimation of Level and Deformed First-Year Sea Ice Surface Roughness in the Canadian Arctic Archipelago from C- and L-Band Synthetic Aperture Radar. *Canadian Journal of Remote Sensing*, *45*(3-4), 457-475. https://doi.org/10.1080/07038992.2019.1647102

Canisius, F., Brisco, B., Murnaghan, K., Van Der Kooij, M., & Keizer, E. (2019). SAR Backscatter and InSAR Coherence for Monitoring Wetland Extent, Flood Pulse and Vegetation: A Study of the Amazon Lowland. *Remote Sensing*, *11*(6), 720.

Dammann, D. O., Eicken, H., Mahoney, A. R., Meyer, F. J., & Betcher, S. (2018). Assessing sea ice trafficability in a changing arctic. *Arctic*, *71*(1), 59. https://doi.org/10.14430/arctic4701

Dammann, D. O., Eriksson, L. E. B., Mahoney, A. R., Eicken, H., & Meyer, F. J. (2019). Mapping pan-Arctic landfast sea ice stability using Sentinel-1 interferometry. *The Cryosphere*, *13*(2), 557-577. https://doi.org/10.5194/tc-13-557-2019

Dierking, W., Lang, O., & Busche, T. (2017). Sea ice local surface topography from single-pass satellite InSAR measurements: a feasibility study. *The Cryosphere*, *11*(4), 1967-1985. https://doi.org/10.5194/tc-11-1967-2017

Drinkwater, M. R., Kwok, R., Rignot, E., Israelsson, H., Onstott, R. G., & Winebrenner, D. P. (1992). Potential Applications of Polarimetry to the Classification of Sea Ice. In *Microwave Remote Sensing of Sea Ice* (pp. 419-430). https://doi.org/https://doi.org/10.1029/GM068p0419

Drinkwater, M. R., & Lytle, V. I. (1997). ERS 1 radar and field-observed characteristics of autumn freeze-up in the Weddell Sea [Article]. *Journal of Geophysical Research-Oceans*, *102*(C6), 12593-12608. https://doi.org/10.1029/97JC00437

Franke, S., Neudert, M., Helm, V., Jutila, A., Hames, O., Neckel, N., Arndt, S., & Haas, C. (2025). Iceberg influence on snow distribution and slush formation on Antarctic landfast sea ice from airborne multi-sensor observations. *EGUsphere*, *2025*, 1-30. https://doi.org/10.5194/egusphere-2025-2657

Fritsen, C. H., Ackley, S. F., Kremer, J. N., & Sullivan, C. W. (1998). Flood-Freeze Cycles and Microalgal Dynamics in Antarctic Pack Ice. In *Antarctic Sea Ice: Biological Processes, Interactions and Variability* (pp. 1-21). https://doi.org/https://doi.org/10.1029/AR073p0001

Gao, F., Wang, X., Gao, Y., Dong, J., & Wang, S. (2019). Sea Ice Change Detection in SAR Images Based on Convolutional-Wavelet Neural Networks. *Ieee Geoscience and Remote Sensing Letters*, *16*(8), 1240-1244. https://doi.org/10.1109/LGRS.2019.2895656

Geilfus, N. X., Delille, B., Tison, J. L., Lemes, M., & Rysgaard, S. (2023). Gas dynamics within landfast sea ice of an Arctic fjord (NE Greenland) during the spring-summer transition [Article]. *Elementa-Science of the Anthropocene*, *11*(1). https://doi.org/10.1525/elementa.2022.00056

Geldsetzer, T., Langlois, A., & Yackel, J. (2009). Dielectric properties of brine-wetted snow on first-year sea ice. *Cold Regions Science and Technology*, *58*(1), 47-56. https://doi.org/https://doi.org/10.1016/j.coldregions.2009.03.009

Gong, M., Li, Y., Jiao, L., Jia, M., & Su, L. (2014). SAR change detection based on intensity and texture changes. *ISPRS Journal of Photogrammetry and Remote Sensing*, *93*, 123-135. https://doi.org/https://doi.org/10.1016/j.isprsjprs.2014.04.010

Gusmeroli, A., & Grosse, G. (2012). Ground penetrating radar detection of subsnow slush on ice-covered lakes in interior Alaska [Article]. *Cryosphere*, *6*(6), 1435-1443. https://doi.org/10.5194/tc-6-1435-2012

Haas, C., Thomas, D. N., & Bareiss, J. (2001). Surface properties and processes of perennial Antarctic sea ice in summer [Article]. *Journal of Glaciology*, *47*(159), 613-625. https://doi.org/10.3189/172756501781831864

Haralick, R. M., Shanmugam, K., & Dinstein, I. (1973). Textural Features for Image Classification. *IEEE Transactions on Systems, Man, and Cybernetics*, *SMC-3*(6), 610-621. https://doi.org/10.1109/TSMC.1973.4309314

Hosseinmostafa, A. R., Lytle, V. I., Jezek, K. C., Gogineni, S. P., Ackley, S. F., & Moore, R. K. (1995). Comparison of Radar Backscatter from Antarctic and Arctic Sea-Ice [Article; Proceedings Paper]. *Journal of Electromagnetic Waves and Applications*, *9*(3), 421-438.

Hosseinmostafa, R., & Lytle, V. (1992, 26-29 May 1992). Comparison of Radar Backscatter from Antarctic and Arctic Sea Ice. [Proceedings] IGARSS '92 International Geoscience and Remote Sensing Symposium,

Hou, B., Wei, Q., Zheng, Y., & Wang, S. (2014). Unsupervised Change Detection in SAR Image Based on Gauss-Log Ratio Image Fusion and Compressed Projection. *Ieee Journal of Selected Topics in Applied Earth Observations and Remote Sensing*, *7*(8), 3297-3317. https://doi.org/10.1109/JSTARS.2014.2328344

Hoyland, K. V. (2009). Ice thickness, growth and salinity in Van Mijenfjorden, Svalbard, Norway [Article]. *Polar Research*, *28*(3), 339-352. https://doi.org/10.1111/j.1751-8369.2009.00133.x

Ikirmiut Community Management Committee. (2023). *Qikiqtarjuaq: Inuit Qaujimajatuqangit Sea Ice Travel Map*.

Jeffries, M. O., Krouse, H. R., Hurst-Cushing, B., & Maksym, T. (2001). Snow-ice accretion and snow-cover depletion on Antarctic first-year sea-ice floes. *Annals of Glaciology*, *33*, 51-60. https://doi.org/10.3189/172756401781818266

Jeffries, M. O., Sek, C. T., & Morris, K. (1995). C-band radar backscatter from antarctic first-year sea ice: I. In situ scatterometer measurements. *Antarctic Journal of the United States*, *30*, 24-26.

Johansson, A. M., Brekke, C., Spreen, G., & King, J. A. (2018). X-, C-, and L-band SAR signatures of newly formed sea ice in Arctic leads during winter and spring. *Remote Sensing of Environment*, *204*, 162-180. https://doi.org/https://doi.org/10.1016/j.rse.2017.10.032

Jutras, M., Vancoppenolle, M., Lourenço, A., Vivier, F., Carnat, G., Madec, G., Rousset, C., & Tison, J. L. (2016). Thermodynamics of slush and snow-ice formation in the Antarctic sea-ice zone [Article]. *Deep-Sea Research Part Ii-Topical Studies in Oceanography*, *131*, 75-83. https://doi.org/10.1016/j.dsr2.2016.03.008

Karlsen, T., Johansson, M., Lohse, J., & Doulgeris, A. P. (2024). Incidence angle dependency and seasonal evolution of L and C-band SAR backscatter over landfast sea ice. *Annals of Glaciology*, *65*, e29, Article e29. https://doi.org/10.1017/aog.2024.30

Kim, J. W., Kim, D. j., & Hwang, B. J. (2012). Characterization of Arctic Sea Ice Thickness Using High-Resolution Spaceborne Polarimetric SAR Data. *Ieee Transactions on Geoscience and Remote Sensing*, *50*(1), 13-22. https://doi.org/10.1109/TGRS.2011.2160070

Lee, J. S., & Pottier, E. (2009). *Polarimetric Radar Imaging: From Basics to Applications* (C. Press, Ed. 1st ed.). https://doi.org/10.1201/9781420054989

Macdonald, G. J., Scharien, R. K., Duncan, K., Farrell, S. L., Rezania, P., & Tavri, A. (2024). Arctic Sea Ice Topography Information From RADARSAT Constellation Mission (RCM) Synthetic Aperture Radar (SAR) Backscatter. *Geophysical Research Letters*, *51*(4), e2023GL107261. https://doi.org/https://doi.org/10.1029/2023GL107261

Mahmud, M. S., Geldsetzer, T., Howell, S. E. L., Yackel, J. J., Nandan, V., & Scharien, R. K. (2018). Incidence Angle Dependence of HH-Polarized C- and L-Band Wintertime Backscatter Over Arctic Sea Ice. *Ieee Transactions on Geoscience and Remote Sensing*, *56*(11), 6686-6698. https://doi.org/10.1109/TGRS.2018.2841343

Mahmud, M. S., Nandan, V., Howell, S. E. L., Geldsetzer, T., & Yackel, J. (2020). Seasonal evolution of L-band SAR backscatter over landfast Arctic sea ice. *Remote Sensing of Environment*, *251*, Article 112049. https://doi.org/10.1016/j.rse.2020.112049

Maillard, P., Clausi, D. A., & Huawu, D. (2005). Operational map-guided classification of SAR sea ice imagery. *Ieee Transactions on Geoscience and Remote Sensing*, *43*(12), 2940-2951. https://doi.org/10.1109/TGRS.2005.857897

Mallett, R., Nandan, V., Stroeve, J., Willatt, R., Saha, M., Yackel, J., Veysière, G., & Wilkinson, J. (2024). Dye tracing of upward brine migration in snow. *Annals of Glaciology*, *65*. https://doi.org/10.1017/aog.2024.27

Marbouti, M., Eriksson, L. E. B., Dammann, D. O., Demchev, D., Jones, J., Berg, A., & Antropov, O. (2020). Evaluating Landfast Sea Ice Ridging near UtqiaġVik Alaska Using TanDEM-X Interferometry. *Remote Sensing*, *12*(8), 1247.

Meyer, F. J., Mahoney, A. R., Eicken, H., Denny, C. L., Druckenmiller, H. C., & Hendricks, S. (2011). Mapping arctic landfast ice extent using L-band synthetic aperture radar interferometry. *Remote Sensing of Environment*, *115*(12), 3029-3043. https://doi.org/https://doi.org/10.1016/j.rse.2011.06.006

Millero, F. J., & Leung, W. H. (1976). The Thermodynamics of Seawater at One Atmosphere. *American Journal of Science*, *276*(9), 1035–1077. https://doi.org/https://doi.org/10.2475/ajs.276.9.1035

Morris, K., & Jeffries, M. (1995). C-band radar backscatter from antarctic first-year sea ice: II. ERS-1 SAR measurements. *Antarctic Journal of the United States*, *30*, 26-28.

Nakamura, K., Wakabayashi, H., Uto, s., Naoki, K., Nishio, F., & Uratsuka, s. (2006). Sea-Ice thickness retrieval in the Sea of Okhotsk using dual-polarization SAR data. *Annals of Glaciology*, *44*, 261-268. https://doi.org/10.3189/172756406781811420

Nandan, V., Scharien, R. K., Geldsetzer, T., Kwok, R., Yackel, J. J., Mahmud, M. S., Rösel, A., Tonboe, R., Granskog, M., Willatt, R., Stroeve, J., Nomura, D., & Frey, M. (2020). Snow Property Controls on Modeled Ku-Band Altimeter Estimates of First-Year Sea Ice Thickness: Case Studies From the Canadian and Norwegian Arctic. *Ieee Journal of Selected Topics in Applied Earth Observations and Remote Sensing*, *13*, 1082-1096. https://doi.org/10.1109/JSTARS.2020.2966432

Nasonova, S., K., S. R., Torsten, G., L., H. S. E., & and Power, D. (2018). Optimal Compact Polarimetric Parameters and Texture Features for Discriminating Sea Ice Types during Winter and Advanced Melt. *Canadian Journal of Remote Sensing*, *44*(4), 390-411. https://doi.org/10.1080/07038992.2018.1527683

Neudert, M., Briggs, R., Bell, T., Hendricks, S., & Haas, C. (2025). Mapping the thickness of slush on sea ice with multi-frequency EM induction sounding. *Cold Regions Science and Technology*, 104767. https://doi.org/https://doi.org/10.1016/j.coldregions.2025.104767

Onstott, T. G., & Shuchman, R. A. (2004). SAR Measurements of Sea Ice. In *Synthetic Aperture Radar Marine User's Manual* (pp. 81-115). U.S. DEPARTMENT OF COMMERCE

Partington, K. C., Flach, J. D., Barber, D., Isleifson, D., Meadows, P. J., & Verlaan, P. (2010). Dual-Polarization C-Band Radar Observations of Sea Ice in the Amundsen Gulf. *Ieee Transactions on Geoscience and Remote Sensing*, *48*(6), 2685-2691. https://doi.org/10.1109/TGRS.2009.2039577

Pedregosa, F., Varoquaux, G., Gramfort, A., Michel, V., Thirion, B., Grisel, O., Blondel, M., Prettenhofer, P., Weiss, R., Dubourg, V., Vanderplas, J., Passos, A., Cournapeau, D., Brucher, M., Perrot, M., & Duchesnay, É. (2011). Scikit-learn: Machine Learning in Python. *J. Mach. Learn. Res.*, *12*(null), 2825–2830.

Pratt, J. W., & Gibbons, J. D. (1981). Kolmogorov-Smirnov Two-Sample Tests. In J. W. Pratt & J. D. Gibbons (Eds.), *Concepts of Nonparametric Theory* (pp. 318-344). Springer New York. https://doi.org/10.1007/978-1-4612-5931-2_7

Provost, C., Sennéchael, N., Miguet, J., Itkin, P., Rösel, A., Koenig, Z., Villacieros-Robineau, N., & Granskog, M. A. (2017). Observations of flooding and snow-ice formation in a thinner Arctic sea-ice regime during the N-ICE2015 campaign: Influence of basal ice melt and storms [Article]. *Journal of Geophysical Research-Oceans*, *122*(9), 7115-7134. https://doi.org/10.1002/2016JC012011

Pulvirenti, L., Chini, M., Pierdicca, N., & Boni, G. (2016). Use of SAR Data for Detecting Floodwater in Urban and Agricultural Areas: The Role of the Interferometric Coherence. *Ieee Transactions on Geoscience and Remote Sensing*, *54*(3), 1532-1544. https://doi.org/10.1109/TGRS.2015.2482001

Richardson, E., Trevizani, R., Greenbaum, J. A., Carter, H., Nielsen, M., & Peters, B. (2024). The receiver operating characteristic curve accurately assesses imbalanced datasets. *Patterns*, *5*(6), 100994. https://doi.org/https://doi.org/10.1016/j.patter.2024.100994

Rignot, E. J. M., & Zyl, J. J. V. (1993). Change Detection Techniques for ERS-1 SAR Data [Article]. *Ieee Transactions on Geoscience and Remote Sensing*, *31*(4), 896-906. https://doi.org/10.1109/36.239913

Risk, C., & James, P. M. A. (2022). Optimal Cross-Validation Strategies for Selection of Spatial Interpolation Models for the Canadian Forest Fire Weather Index System. *Earth and Space Science*, *9*(2), e2021EA002019. https://doi.org/https://doi.org/10.1029/2021EA002019

Rösel, A., Farrell, S. L., Nandan, V., Richter-Menge, J., Spreen, G., Divine, D. V., Steer, A., Gallet, J. C., & Gerland, S. (2021). Implications of surface flooding on airborne estimates of snow depth on sea ice [Article]. *Cryosphere*, *15*(6), 2819-2833. https://doi.org/10.5194/tc-15-2819-2021

https://doi.org/10.5194/egusphere-2026-4311
Preprint. Discussion started: 23 July 2026

Saloranta, T. M. (2000). Modeling the evolution of snow, snow ice and ice in the Baltic Sea [Article]. *Tellus Series a-Dynamic Meteorology and Oceanography*, *52*(1), 93-108. https://doi.org/10.1034/j.1600-0870.2000.520107.x

Scharien, R. K., Geldsetzer, T., Barber, D. G., Yackel, J. J., & Langlois, A. (2010). Physical, dielectric, and C band microwave scattering properties of first-year sea ice during advanced melt. *Journal of Geophysical Research: Oceans*, *115*(C12). https://doi.org/https://doi.org/10.1029/2010JC006257

Scharien, R. K., Hochheim, K., Landy, J., & Barber, D. G. (2014a). First-year sea ice melt pond fraction estimation from dual-polarisation C-band SAR - Part 2: Scaling in situ to Radarsat-2 [Article]. *Cryosphere*, *8*(6), 2163-2176. https://doi.org/10.5194/tc-8-2163-2014

Scharien, R. K., Landy, J., & Barber, D. G. (2014b). First-year sea ice melt pond fraction estimation from dual-polarisation C-band SAR – Part 1: In situ observations. *The Cryosphere*, *8*(6), 2147-2162. https://doi.org/10.5194/tc-8-2147-2014

Scharien, R. K., Segal, R., Yackel, J. J., Howell, S. E. L., & Nasonova, S. (2018). Linking winter and spring thermodynamic sea-ice states at critical scales using an object-based image analysis of Sentinel-1. *Annals of Glaciology*, *59*(76pt2), 148-162. https://doi.org/10.1017/aog.2017.43

Scharien, R. K., Yackel, J. J., Barber, D. G., Asplin, M., Gupta, M., & Isleifson, D. (2012). Geophysical controls on C band polarimetric backscatter from melt pond covered Arctic first-year sea ice: Assessment using high-resolution scatterometry. *Journal of Geophysical Research: Oceans*, *117*(C9). https://doi.org/https://doi.org/10.1029/2011JC007353

Scheuchl, B., Flett, D. G., Abreu, R. d., & Arkett, M. (2004). THE POTENTIAL OF CROSS-POLARIZATION INFORMATION FOR OPERATIONAL SEA ICE MONITORING.

Segal, R. A., Scharien, R. K., Cafarella, S., & Tedstone, A. (2020a). Characterizing winter landfast sea-ice surface roughness in the Canadian Arctic Archipelago using Sentinel-1 synthetic aperture radar and the Multi-angle Imaging SpectroRadiometer. *Annals of Glaciology*, *61*(83), 284-298. https://doi.org/10.1017/aog.2020.48

Segal, R. A., Scharien, R. K., Duerden, F., & Tam, C. L. (2020b). The Best of Both Worlds: Connecting Remote Sensing and Arctic Communities for Safe Sea Ice Travel [Article]. *Arctic*, *73*(4), 461-484. https://doi.org/10.14430/arctic71567

Shepard, D. (1968). A two-dimensional interpolation function for irregularly-spaced data. Proceedings of the 1968 23rd ACM national conference,

Shokr, M., & Dabboor, M. (2024). Angular variation of SAR polarimetric parameters over multiyear ice. *International Journal of Remote Sensing*, *45*(22), 7996-8014. https://doi.org/10.1080/01431161.2024.2394237

Soh, L.-K., & Tsatsoulis, C. (1999). Texture analysis of SAR sea ice imagery using gray level co-occurrence matrices. *IEEE Trans. Geosci. Remote. Sens.*, *37*, 780-795.

Sujon, K. M., Hassan, R., Choi, K., & Samad, M. A. (2025). Accuracy, precision, recall, f1-score, or MCC? empirical evidence from advanced statistics, ML, and XAI for evaluating business predictive models. *Journal of Big Data*, *12*(1), 268. https://doi.org/10.1186/s40537-025-01313-4

Wakabayashi, H., Matsuoka, T., Nakamura, K., & Nishio, F. (2004). Polarimetric Characteristics of sea ice in the sea of Okhotsk observed by airborne L-band SAR. *Ieee Transactions on Geoscience and Remote Sensing*, *42*(11), 2412-2425. https://doi.org/10.1109/TGRS.2004.836259

Williams, J. C. B., Ackley, S., Mestas-Nuñez, A. M., Macdonald, G. J., & Arndt, S. (2024). Detection of sea ice floe flooding in the Southern Ocean using Sentinel-1 SAR imagery [Preprint]. *EarthArXiv*. https://doi.org/10.31223/X53T2C

Wilson, K. J., Arreak, A., Itulu, J., Sikumiut Community Management, C., Ljubicic, G. J., & Bell, T. (2021). "When We're on the Ice, All We Have is Our Inuit Qaujimajatuqangit"

Mobilizing Inuit Knowledge as a Sea Ice Safety Adaptation Strategy in Mittimatalik, Nunavut. *Arctic*, *74*(4), 525-549. https://www.jstor.org/stable/27110558

Yackel, J., Geldsetzer, T., Yendamuri, K., Nandan, V., Tonboe, R., Stroeve, J., Saha, M., Mallett, R., & Lam, H. M. (2026). Observations of Coherence Changes in C-Band SAR Linked to Snow Thermodynamics and Wind Redistribution on First-Year Sea Ice. *Geophysical Research Letters*, *53*(7), e2025GL121597. https://doi.org/https://doi.org/10.1029/2025GL121597

Yackel, J. J., Barber, D., Papapkyriakou, T., & Breneman, C. (2007). First-year sea ice spring melt transitions in the Canadian Arctic Archipelago from time-series synthetic aperture radar data, 1992–2002. *Hydrological Processes*, *21*, 253-265. https://doi.org/10.1002/hyp.6240

https://doi.org/10.5194/egusphere-2026-4311
Preprint. Discussion started: 23 July 2026

Zhou, L., Stroeve, J., Nandan, V., Willatt, R., Xu, S. M., Zhu, W. X., Kacimi, S., Arndt, S., & Yang, Z. F. (2024). Quantifying the influence of snow over sea ice morphology on L-band passive microwave satellite observations in the Southern Ocean. *Cryosphere*, *18*(9), 4399-4434. https://doi.org/10.5194/tc-18-4399-2024